Faculty of Science

Physics Institute

Bachelor Thesis

Estimation of Energy Scales in the Spin-1/2 Dimer Compound $Ba_{3-x}Sr_xCr_2O_8$ from Heat Capacity Measurements

Group:
Prof. Dr. Andreas Schilling

Supervisor:
Alsu Gazizulina

Author:
Michele Masseroni

March, 2017

Abstract

Strontium chromium oxide ($Sr_3Cr_2O_8$) and barium chromium oxide ($Ba_3Cr_2O_8$) are three-dimensional weakly coupled spin-$^1/_2$ dimer systems. They are characterised by magnetic Cr^{5+} ($3d^1$,$s = {}^1/_2$) ions, which upon interaction form dimers with a dominant intra-dimer coupling constant (J_0). As a consequence, a singlet ground state ($S = 0$) and a triplet excited state ($S = 1$) are formed, their energy difference corresponds to the spin gap (Δ). In order to study the magnetic properties of the system, the spin gap has to be quantified. Commonly, this is done by performing inelastic neutron scattering (INS) experiments. Interestingly, the energy gap may also be estimated by a heat capacity measurement. In fact the thermal excitation of spin dimers appears like a broad peak in the heat capacity (Schottky anomaly), which shape and position depend on the energy gap Δ.

The aim of this work is the investigation of the heat capacity as a valid technique for the estimation of the energy gap in a three-dimensional spin dimer system. Indeed, this technique is a simpler way than INS and it could be accessible in many laboratories. To do this, we firstly prepared polycrystalline samples of $Ba_{3-x}Sr_xCr_2O_8$ and tested the resulting materials with x-ray diffraction. The pattern intensities were described by the hexagonal space group $R\bar{3}m$. The lattice parameters $a = b$ and c agreed with the values of previous publications [1, 2] for $x = \{0, 3\}$, and they were linearly dependent on the Sr content (x), indicating the successful preparation of the samples. Finally, we measured the heat capacity and extrapolated the energy gap Δ by fitting the data with a theoretical model, which takes into account the lattice, orbital and magnetic contributions.

For $Sr_3Cr_2O_8$, the fit of the Schottky anomaly leads to the energy 5.42 meV, which is in contrast with the value obtained by INS (3.5 meV) [3]. Similarly, we measured the energy gap for $Ba_3Cr_2O_8$ leading to a value of 2.38 meV, while a high-field magnetisation measurement reported 1.4 meV [4]. Our results show that the value of the energy obtained from heat capacity measurements do not correspond to the energy gap between the singlet and triplet state. This discrepancy is caused by the inter-dimer interactions that induce a dispersion in the excited state and thus a bandwidth in the triplet state. While the gap is reduced by the three dimensional interactions, the fitted gap has the magnitude of the energies in the center of the band. We suppose that a density of states weights the thermal excitations, such that the excitations have preference for the energies in the center of the band and not for the lowest available energies. In fact, both results for $x = 0$ and $x = 3$ are in agreement with the center of the excitation spectrum determined by INS [3, 5]. Therefore, we define energy obtained by fitting the data as the effective gap (Δ_{eff}). It corresponds to the spin gap $\Delta = J_0$ only for isolated dimers (where the energy levels are sharp), and for weakly interacting dimers, we suspect that it could be identified as the interaction constant, i. e. $\Delta_{\text{eff}} \approx J_0$. Effectively, our results are in agreement with the values of the interaction constants determined by INS, 5.55 meV [3] and 2.38 meV [6] for $Sr_3Cr_2O_8$ and $Ba_3Cr_2O_8$, respectively. However, for intermediated Sr content ($x = 1.5$ and $x = 2.7$), the exchange constants obtained by magnetisation measurements [7] are smaller than the energies obtained by the heat capacity, especially in the case of $Ba_{1.5}Sr_{1.5}Cr_2O_8$.

In conclusion, our results suggest that the heat capacity measurement could be a valid approach to the estimation of the energy scales of a weakly interacting dimer system. However, this technique does not allow to determine the energy gap of the spin dimer system. Anyway, further experiments are needed to prove the reliability of the results for intermediated steps of Sr content.

Contents

1 Introduction

Bose-Einstein condensation (BEC) is one of the most interesting exotic states of matter studied by condensed matter physics. At very low temperatures, the bosons of a system condense into a collective ground state, causing macroscopic effects, such as superfluidity in ^{4}He. Besides cooled atomic gases [8], a BEC related quantum phase transition was observed also in dimerized (i.e. with paired spins) spin-$^1/_2$ systems [9]. Such a system has two energy levels separated by an energy gap Δ: a non-magnetic singlet ground state ($S = 0$, where S is the total spin) and a threefold degenerated triplet state ($S = 1$). Because of the integer spin, the excitations can be described like a bosonic quasi-particles called triplons. At the temperature of 0 K, the dimers are in the ground state and the density of the triplons is zero. By applying an external magnetic field H, the degeneracy of the excited state is removed (Zeeman effect), reducing the energy gap between the ground and the first excited state ($S_z = -1$, where $z \parallel H$). At the critical field H_c, the lower branch of the triplet state merges with the ground state, becoming energetic favourable, and leading to triplon condensation. Since the triplons are weakly interacting, they do not suddenly condense altogether. In fact, their density can be controlled by the strength of the magnetic field $H > H_c$, until saturation is reached [10]. The phenomenon of BEC was experimentally confirmed in the magnetic insulator $TlCuCl_3$ in 2000 [9], and recently, this quantum phase transition was observed also in $Ba_3Cr_2O_8$ [11] and $Sr_3Cr_2O_8$ [12]. The last two compounds are isostructural, exhibiting a hexagonal crystalline structure with space group $R\bar{3}m$ (Figure 1) [1, 2]. In these compounds, the Cr ions are in the rare oxidation state 5+, enclosed in an oxygen tetrahedron. The $3d$ orbital is occupied by a single electron, thus the Cr^{5+} ions carry the spin $s = {}^1/_2$. The Cr ions interact antiferromagnetically with adjacent Cr ions along the c axis and form a hexagonal lattice of dimers (black ellypse in Figure 1) in an $ABCABC$ arrangement [6]. The interactions are characterized by a dominant intra-dimer interaction constant J_0. For an isolated dimer, the spin gap is identical to J_0, whereas the inter-dimer interactions cause a dispersive excited state [6, 3], reducing the gap.

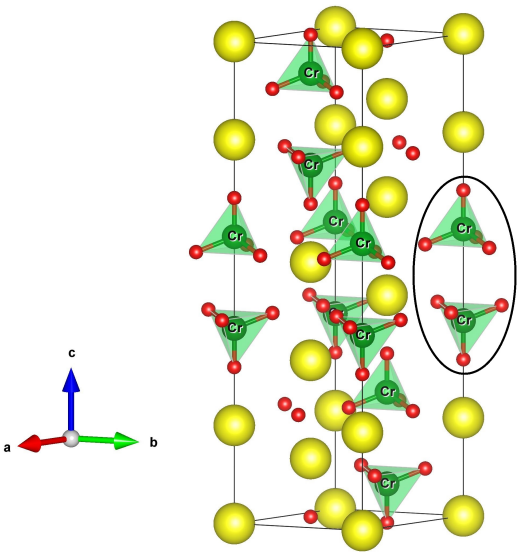

Figure 1: Crystal structure of $Sr_3/Ba_3Cr_2O_8$. The Sr/Ba, Cr and O ions are represented by yellow, green and red spheres, respectively. The oxygen tetrahedrons with Cr^{5+} ions in the middle are highlighted. A dimer is marked with a black ellipse. The picture was edited with the program VESTA.

A useful technique used to study the magnetic excitations is the inelastic neutron scattering (INS). However, this is a complicated technique and requires the preparation of relatively large amounts of single crystal, which is not always possible. Since in the thermal processes, such as the spin dimer excitations, the first populated excited levels are the lowest possible, we supposed that the heat capacity could be a valid alternative to INS in the estimation of the energy gap Δ. In fact, the excitation of the spin dimers appears like a Schottky anomaly in the heat capacity, which can be fitted by a well known theoretical model, leading to the spin gap.

In order to verify our hypothesis, we prepared polycrystalline samples. There are several preparation methods, using the solid state reactions in air [13, 12] or flowing Argon [3, 14, 1], which differ to each

other in the time and temperature of the heating procedure as well as in the cooling down. We opted for a solid state reaction in air as reported in Chapter 3.1. The resulting materials were analysed with x-ray powder diffraction. We performed x-ray powder diffraction to assess the result of our preparation method. As expected, the intensity pattern of all samples was well fitted by the hexagonal space group $R\bar{3}m$. The lattice parameters ($a = b$ and c) of $Sr_3Cr_2O_8$ and $Ba_3Cr_2O_8$ were compared with previous publications [1, 2], which reported similar values. For intermediate Sr contents x, we verified the linear dependence of the cell parameters on the percentage of strontium (Vegard's law). Afterwords we performed heat capacity measurements and fitted the data with a theoretical model, taking into account the phonon contribution, the electron orbital contribution, and the magnetic (or spin) contribution. In contrast to the expectation, the fit of the Schottky anomaly (due to the excitation of the spin dimers) shows that the fitted energy is not comparable with the energy gap. Therefore, we define the effective energy gap Δ_{eff} that is the energy obtained by fitting the Schottky anomaly. This quantity can be interpreted as a weighted mean value of the energies available in the excited band and it could be closely related to the exchange constant J_0.

The thesis is structured as follows. In Chapter 2, we explain the basic principles of the heat capacity: its definition and the factors that affect it (lattice, orbital and magnetic contributions). In Chapter 3, we report the preparation method of the samples and the equipment involved in the measurement of the x-ray diffraction (XRD) pattern and the heat capacity. The results are presented in Chapter 4, where we discuss the fitting procedure of the molar heat capacity and briefly show the magnetic dependence of ΔC. The conclusions of this work are reported in Chapter 5.

2 Physical Principle

2.1 Concepts of Thermodynamics

The first law of thermodynamics describes the principle of energy conservation in thermodynamic systems, which takes into account the heat as a form of energy [15]. For an isolated system, this law can be written as

$$dU = \delta Q + \delta W, \tag{1}$$

where U denotes the internal energy, while Q and W represent respectively the quantity of heat and the work supplied to the system. The heat capacity is defined as the ratio between added heat and the variation of the system's temperature

$$C_x = \left.\frac{\partial Q}{\partial T}\right|_x, \tag{2}$$

where x is a state variable that is kept constant when the temperature is varied. Defining the work as $W = -pdV$, it follows that the term δW in (1) disappears for constant volumes. As a result, the heat capacity can be defined as

$$C_{\mathrm{V}} = \left.\frac{\partial U}{\partial T}\right|_{\mathrm{V}}. \tag{3}$$

Commonly, the heat capacity of solids is measured at a constant pressure (C_{p}). From equation (1), the relation $C_{\mathrm{p}} > C_{\mathrm{V}}$ can be derived. However, the difference between C_{P} and C_{V} is really small at room temperatures and is negligible at cryogenic temperatures [16]. Therefore, the definition (3) is usually used to described the experimental data.

The heat capacity is an extensive property, *i. e.* it depends on the size of the system. On the contrary, the specific heat capacity $c = C_x/m$ (m is the mass of the sample) and the molar heat capacity $C_x^{\mathrm{mol}} = C_x/n$ (n is the numbers of moles) are intensive properties. In this work, we analyse the molar heat capacity, which we denote as C to make it easily legible.

2.2 Analysis of Heat Capacity Data

When heat is added to a system, a part of this energy is used to activate thermal processes, such as lattice vibrations, electron excitations into conduction bands (in conductors and semi-conductors), the excitation of magnons (ferri-, ferro- and antiferro-magnetic materials), etc. The changes in the heat capacity are attributed to those thermal phenomena and the total heat capacity is the sum of the single contributions ΔC [16]

$$C_{\mathrm{tot}} = \sum_i \Delta C_i. \tag{4}$$

In the specific case of the antiferromagnetic insulator $Ba_{3\text{-}x}Sr_xCr_2O_8$, which we studied, three factors contribute to its heat capacity

$$C = C_{\mathrm{latt}} + C_{\mathrm{mag}} + C_{\mathrm{oo}}. \tag{5}$$

C_{latt} is the lattice contribution due to the vibration modes of the ions, C_{mag} is the magnetic contribution caused by the spin excitation of the spin-dimers Cr^{5+}-Cr^{5+} (triplons), and C_{oo} is attributed to orbital degrees of freedom of the electron in the $3d^1$ orbital of the Cr^{5+} ions (Chapter 2.4) [17, 18].

2.3 Lattice Heat Capacity

The thermal energy of the crystals is the energy stored in form of ionic thermal motions around their equilibrium positions (lattice vibrations). According to the classical theory, the lattice heat capacity is expressed by the Dulong-Petit law, which states $C = 3R$, where R is the universal gas constant ($R = 8.314\,\frac{\mathrm{J}}{\mathrm{Kmol}}$). This is consistent with the experimental data for most of the crystals as long as one is just interested in the heat capacity around room temperatures [16]. However, for temperatures approaching 0 K, the measurements show that the heat capacity converges to zero. Given this background, a quantum mechanical approach to the vibration modes is needed in order to describe the discrepancy between the theoretical value and the experimental behaviour of the heat capacity.

2.3.1 The Einstein Model

Einstein considered a system of independent oscillators with frequency ν_{E}, where only the energy states $\varepsilon_n = nh\nu_{\mathrm{E}}$ are available [19]. The partition function of such system is given by

$$Z = \sum_{n=0}^{\infty} e^{-\beta n h \nu_{\mathrm{E}}} = \frac{1}{1 - e^{-\beta h \nu_{\mathrm{E}}}}, \tag{6}$$

where $\beta = 1/k_{\mathrm{B}}T$ and k_{B} is the Boltzmann constant ($k_{\mathrm{B}} = 8.617 \times 10^{-5}\ \frac{\mathrm{eV}}{\mathrm{K}}$). The relation $\langle \varepsilon \rangle = -\frac{d}{d\beta} \ln(Z)$ leads to the mean energy of the vibrational modes

$$\langle \varepsilon \rangle = \frac{h\nu}{e^{\beta h \nu_{\mathrm{E}}} - 1}. \tag{7}$$

Assuming N to be the number of atoms in a crystal and three degrees of freedom for each vibration's mode, the internal energy is given by

$$U = 3N \langle \varepsilon \rangle = 3N \frac{h\nu}{e^{\beta h \nu_{\mathrm{E}}} - 1}, \tag{8}$$

and the definition (3) leads to the molar heat capacity

$$C_{\mathrm{E}} = 3R \left(\frac{\Theta_{\mathrm{E}}}{T} \right)^2 \frac{e^{\frac{\Theta_{\mathrm{E}}}{T}}}{\left(e^{\frac{\Theta_{\mathrm{E}}}{T}} - 1 \right)^2}, \tag{9}$$

where $\Theta_{\mathrm{E}} = h\nu_{\mathrm{E}}/k_B$ is the Einstein Temperature.

Because Einstein's model assumes a single frequency, excluding the low frequency modes, the heat capacity rapidly decreases in the $T \to 0$ limit. In fact, whereas the experimental data show a polynomial decrease of T^3, the Einstein's model converges asymptotically with $\frac{1}{T^2} e^{-1/T}$ (Figure 2).

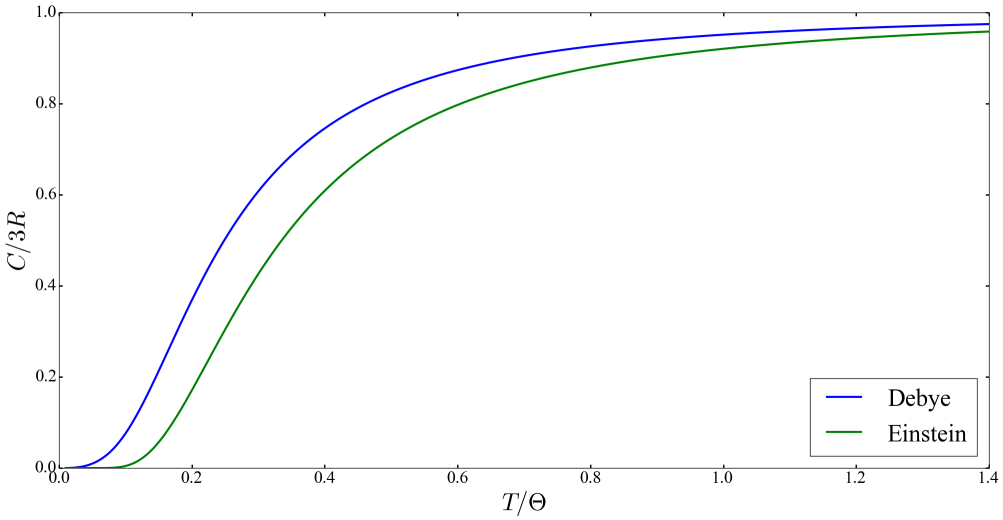

Figure 2: The Debye and Einstein models of the lattice heat capacity.

2.3.2 The Debye Model

To avoid the problems of Einstein's model, Debye proposed another model for the heat capacity [20]. This model takes into account elastic waves with linear dispersion relation $\omega = vk$, where v is the propagation velocity and k is the wave vector [19]. The number of possible modes is fixed by the maximal value of $3N$, where N is the number of atoms and the factor 3 describes the three acoustic modes (two transversal and one longitudinal). This leads to a maximal frequency: the Debye frequency ω_{D}.

The internal energy is given by the following sum

$$U = \sum_{i=1}^{3} \sum_{k} \frac{h\omega_i(k)}{e^{\beta h \omega_i(k)} - 1}. \tag{10}$$

With the assumption of a continuum of states k, the sum over all wave vectors can be modified into an integral over the frequencies ω. The integration is weighted by a density of states $D(\omega)$ (the number of states in the interval $[\omega, \omega + d\omega]$). In k-space, there is exactly one state in the volume $(2\pi)^3/V$ (V is the volume of the sample). The number of states with wave vector smaller than k is given by

$$N_k = \frac{V}{(2\pi)^3} \underbrace{\frac{4\pi k^3}{3}}_{\substack{\text{volume of a sphere} \\ \text{with radius } k}} . \tag{11}$$

The definition $D(\omega) = \frac{dN_k}{d\omega}$ together with the dispersion relation $\omega = vk$ leads to

$$D(\omega) = \frac{V\omega^2}{2\pi^2 v^3}. \tag{12}$$

The sum over the three acoustic modes can be substituted by the definition of the mean propagation velocity [21]

$$\frac{1}{v_s} = \frac{1}{3}\sum_{i=1}^{3} \int \frac{d\Omega}{4\pi} \frac{1}{v_i^3}. \tag{13}$$

The internal energy can be integrated according to the equation

$$U = \int_0^{\omega_D} d\omega \left(\frac{V\omega^2}{2\pi^2 v_s^3}\right)\left(\frac{\hbar\omega}{e^{\beta\hbar\omega} - 1}\right). \tag{14}$$

The derivative of the energy with respect to the temperature leads to the heat capacity

$$C_{\mathrm{D}} = 9R\left(\frac{T}{\Theta_{\mathrm{D}}}\right)^3 \int_0^{\Theta_{\mathrm{D}}/T} dx \frac{x^4 e^x}{(e^x - 1)^2}, \tag{15}$$

where $x = \frac{\hbar\omega}{k_{\mathrm{B}}T}$, and $\Theta_{\mathrm{D}} = \frac{\hbar\omega_{\mathrm{D}}}{k_{\mathrm{B}}}$ is the Debye temperature [20].

At high temperatures, Equation (15) converges to the Dulong-Petit law. At low temperatures, the integral gives the result of $\pi^4/15$. Consequently, C_{D} is proportional to T^3, in agreement with the experimental data. In contrast to the predictions, the Debye temperature of solids is not constant, but varies depending on the temperature. This incongruity may be a consequence of the assumptions of the model [16]. In Figure 2, the behaviour of the Debye and Einstein models are compared.

2.3.3 The Lattice Contribution in the $Ba_{3-x}Sr_xCr_2O_8$ Solid Solution

According to the publications of Wang *et al* [17, 18], the lattice contribution to the specific heat of $Sr_3Cr_2O_8$ and $Ba_3Cr_2O_8$ can be modelled as the sum of one Debye D (Equation 15) and four Einstein E_1, E_2, E_3, E_4 terms (Equation 9). The elements of this sum have the ratio $D : E_1 : E_2 : E_3 : E_4 = 1 : 3 : 4 : 3 : 2$, for a total of 39 degrees of freedom per formula unit. The characteristic temperatures (Table 1) were modelled to fit the experimental data and were compared to the IR active phonons spectrum.

	Θ_{D}	Θ_{E1}	Θ_{E2}	Θ_{E3}	Θ_{E4}
$Sr_3Cr_2O_8$	135.5	153.4	306.2	541.6	1360
$Ba_3Cr_2O_8$	123	137	265	658	1270

Table 1: Temperatures of the lattice model used to describe the phonon contribution to the specific heat of $Sr_3Cr_2O_8$ and $Ba_3Cr_2O_8$. All temperatures are given in Kelvin [K].

In order to study the magnetic contribution to the heat capacity of $Ba_{3-x}Sr_xCr_2O_8$, the lattice contribution has to be subtracted from the heat capacity. Starting from the model of Wang *et al.*, we used an interpolation method suggested by Prof. Dr. Schilling [22] (details in Appendix) to model the theoretical curve of the heat capacity for different Sr content x. The interpolation based on the mass and unit cell volume dependence of the Debye (or Einstein) temperature

$$T_B = T_A\sqrt{\frac{M_A V_A}{M_B V_B}}, \tag{16}$$

where A and B are two isostructural compounds with similar chemical properties. From this scale factor, it follows

$$C_x(T) = \epsilon_x C_{x=3}(T) + (1-\epsilon_x) C_{x=0}(T), \tag{17}$$

where

$$\epsilon_x = \frac{(M_x V_x)^{-1/2} - (M_{x=3} V_{x=3})^{-1/2}}{(M_{x=0} V_{x=0})^{-1/2} - (M_{x=3} V_{x=3})^{-1/2}}. \tag{18}$$

In the last equation, M_x and V_x are respectively the molar mass and unit cell volume (obtained by XRD) of $Ba_{3-x}Sr_xCr_2O_8$. We compared this method with the Kopp-Neumann (KN) law [16], which states

$$C_x = \frac{3-x}{3} C_{x=0} + \frac{x}{3} C_{x=3}. \tag{19}$$

The two method are essentially equivalent, since their difference is about 1 % for $x = 1.5$ (calculated for the Debye term) and even smaller for the other x values. The advantage of the KN law is that one does not need to perform XRD to obtain the unit cell volume.

The theoretical curves modelled by Wang *et al.* described only approximatively our data. Consequently, also the curves obtained with the interpolation did not match well to the data. Therefore, we fitted the lattice contribution

$$C_{\text{latt}} = D + 3 \cdot E_1 + 4 \cdot E_2 + 3 \cdot E_3 + 2 \cdot E_4. \tag{20}$$

For each term, there is one free parameter (Debye or Einstein temperature). These characteristic temperatures are not well separated in the temperature scale, consequently, they are correlated to each other, especially the Debye D and Einstein $E1$. For this reason, we choose carefully the start parameters, using the temperatures obtained by Wang *et al.* for the parent compounds, and using Equation (16) for the intermediate Sr content x. For some compounds, both the fit and the interpolated curve describe well the data at high temperatures, while to obtain a good fit of the magnetic contribution, the characteristic temperatures needed to be refined. Therefore, we discuss in the conclusion only the results obtained by the fit of the experimental data.

2.4 Schottky Anomaly

The heat capacity contribution due to thermal excitations in a multilevel system is called Schottky anomaly. Ordinarily, it is observed at very low temperatures, where other contributions are small. For a n-level system with energies ε_i $(0 \leq i \leq n)$, the partition function is given by

$$Z = \sum_{i=0}^{n} g_i e^{-\beta \varepsilon_i}, \tag{21}$$

where g_i is the degeneracy of the i-th energy level [16]. For simplicity, the energy of the ground state is set to $\varepsilon_0 = 0$, and the energy ε_i is the difference between the ground state and the i-th excited state. The mean energy is obtained from the equation $\langle E \rangle = -\frac{d}{d\beta} \ln Z$,

$$\langle E \rangle = \frac{1}{Z} \sum_{i=0}^{n} g_i \varepsilon_i e^{-\beta \varepsilon_i}, \tag{22}$$

and the resulting molar heat capacity is given by

$$C_{\text{Sch}}(T) = R\beta^2 \left(\langle E^2 \rangle - \langle E \rangle^2 \right), \tag{23}$$

where $\langle E^2 \rangle = Z^{-1} \sum_{i=0}^{n} g_i \varepsilon_i^2 e^{-\beta \varepsilon_i}$.

2.4.1 The Schottky Anomaly of a Spin Quantum Dimer

Upon spin coupling, a spin dimer is formed, as in the case of two adjacent Cr ions in the $Ba_{3-x}Sr_xCr_2O_8$ compound. Assuming $s_{1,2}$ and J_0 to be respectively the spins of the ions and the interaction constant, the Hamiltonian of the isolated dimer is given by

$$\hat{H} = \frac{J_0}{\hbar^2} \vec{s_1} \cdot \vec{s_2} = \frac{J_0}{2\hbar^2} (\vec{S}^2 - \vec{s_1}^2 - \vec{s_2}^2) = \frac{J_0}{2\hbar^2} \left[S(S+1) - 2s(s+1) \right], \tag{24}$$

where S is the total spin of the system and $s = 1/2$ [23]. The total spin quantum numbers are $S = 0$ ($|0,0\rangle$) for the singlet ground state and $S = 1$ ($\{|1,1\rangle, |1,0\rangle, |1,-1\rangle\}$) for the triplet excited states.[1] Applying the Hamilton operator on the eigenstates, one gets the eigenvalues of the energy states, which are $-3/4 J_0$ and $1/4 J_0$, for the ground and the excited states, respectively. Thus, the energy levels are separated by an energy gap $\Delta = J_0$ (Figure 3).

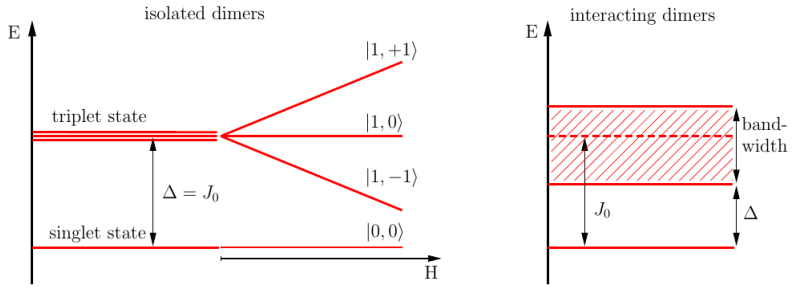

Figure 3: Energy states of an isolated spin-1/2 dimer system (left) and a weakly interacting spin dimer system (right). In the first case, the ground state is separated from the threefold excited state by an energy gap $\Delta = J_0$. The threefold degeneracy of the excited state is removed by an external magnetic field H (Zeeman effect). In the second case, the excited state is a threefold degenerated band. The energy gap is reduced ($\Delta < J_0$) due to the inter-dimer interactions.

The Schottky anomaly of this system can be derived from Equation (23), using the partition function $Z = 1 + 3e^{-\beta\Delta}$. The resulting molar heat capacity is

$$C_{\text{mag}} = n_d R(\beta\Delta)^2 \frac{3e^{-\beta\Delta}}{(1+3e^{-\beta\Delta})^2}, \tag{25}$$

where n_d represents the fraction of dimerized Cr^{+5} ions ($0 < n_d < 1$). Since the peak height of the Schottky anomaly is related to the number of dimers in the sample, a smaller peak indicates that a certain percentage of chromium ions are not dimerized, consequently $n_d < 1$. This factor was firstly introduced by Grundmann in the fit of his magnetisation measurements [7]. The model used to fit the experimental data consists of the sum of a Bleaney-Bowers term (M_d) and a Brillouin term (M_p). The first term describes the magnetisation of the dimers, thus it is multiplied by the factor n_d. While the second term describes the paramagnetic background and is multiplied by another factor n_p, where n_p is the fraction of free Cr ions. Grundmann found out that the paramagnetic component becomes more relevant for the Sr content x around 1.3 (Figure 4). Our heat capacity measurement are in agreement with the results of the magnetisation measurements. Indeed, the Schottky anomaly of $Ba_{1.5}Sr_{1.5}Cr_2O_8$ was notably smaller than for the other Sr content.

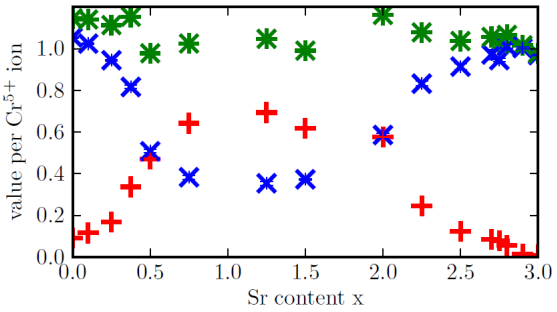

Figure 4: Estimated fraction of dimerized n_d (blue crosses) and free n_p (red plus symbols) Cr^{5+} ions from a magnetisation measurement as a function of the Sr content x. The sum of these fractions is represented by the green asterisks. (Figure retrieved from Ref. [7])

On the contrary, the position of the maximum is not affected by the number of dimerized ions. In fact, it is determined only by the magnitude of the energy gap Δ, thus it provides a first estimation of the spin

[1] The notation used to describe the spin states is $|s,m\rangle$, where s indicate the spin quantum number and m the magnetic quantum number.

gap. Using the necessary condition of a maximum $\frac{dC}{dT} = 0$ in Equation (25), one gets the equation

$$2(1 + 3e^{-x}) + x(3e^{-x} - 1) = 0, \tag{26}$$

where $x = \beta\Delta$. The numerical solution of this equation leads to the factor $x \approx 2.845$. The temperature, for which the heat capacity reaches the maximal value, increases linearly with the magnitude of the interaction constant and is given by

$$T_{\max} = \frac{\Delta}{k_{\mathrm{B}} x} \approx 4.079 \cdot \Delta[\mathrm{meV}]. \tag{27}$$

By applying an external magnetic field H, the degeneracy of the triplet state is removed (Zeeman effect) [7] (Figure 3). Because the energy of the ground state is not affected by the magnetic field (i. e. $\varepsilon_0 = 0$), the energies of the excited state are given by

$$\varepsilon_{1,2,3} = \Delta + mg\mu_{\mathrm{B}} H, \tag{28}$$

where $m = \{1, 0, -1\}$, g is the Landé-factor and μ_{B} is the Bohr magneton. The Schottky anomaly is given by Equation (23), using the partition function

$$Z = \sum_{i=0}^{3} e^{-\beta\varepsilon_i}. \tag{29}$$

Figure 5 shows the theoretical curve C_{mag}/T as a function of the temperature for different magnetic fields. The increase of the Schottky anomaly starts at lower temperatures for higher magnetic fields, because the excited state with magnetic quantum number $m = -1$ gets closer to the ground state (Figure 5). In addition, the peak height decreases and the position of the maximum shift to lower temperatures.

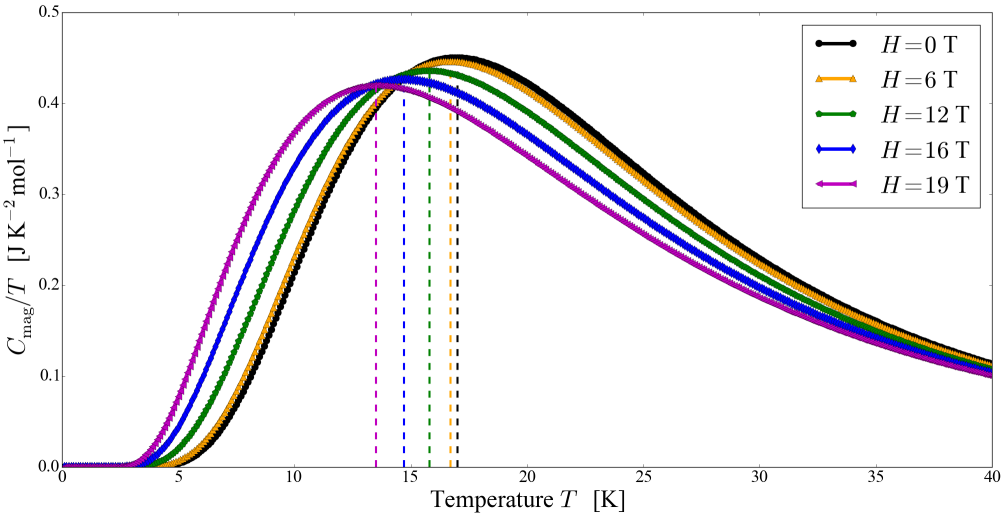

Figure 5: Theoretical heat capacity C_{mag}/T of an isolated spin-dimer system as a function of the temperature T for various magnetic fields. The energy gap used in the picture is $\Delta = 5.26\,\mathrm{meV}$ and corresponds to the estimated gap of $Ba_{0.1}Sr_{2.9}Cr_2O_8$.

Actually, the dimers are not isolated but rather interact with adjacent dimers. Consequently, the excited state is dispersive and has a finite bandwidth [6, 3] (Figure 3). To investigate how the triplon dispersion affects the Schottky anomaly, we introduced a density of states (DOS) $D(\varepsilon)$. We approximated the density of states by a Gaussian distribution, with center at $\mu(J_0, m, H) = J_0 + mg\mu_{\mathrm{B}} H$ and standard deviation $\sigma = \frac{\delta}{6}$, where δ is the bandwidth (to count 99.7 % of the states within the bandwidth)

$$D(\varepsilon, H) = \frac{1}{\sqrt{2\pi\sigma^2}} e^{-\frac{(\varepsilon - J_0 + mg\mu_{\mathrm{B}} H)^2}{2\sigma^2}}. \tag{30}$$

With this definition, we modified the partition function to

$$Z = 1 + \sum_{m=-1}^{1} \int_0^\infty \mathrm{d}\varepsilon D(\varepsilon, H) e^{-\beta\varepsilon}, \tag{31}$$

and the mean energy to

$$\langle E \rangle = \frac{1}{Z} \sum_{m=-1}^{1} \int_{0}^{\infty} \mathrm{d}\varepsilon D(\varepsilon, H)\ \varepsilon\ e^{-\beta\varepsilon}. \tag{32}$$

Finally, we obtained the Schottky anomaly by inserting (32) in Equation (25) and then performing a numerical integration.

As an example, we plotted the theoretical Schottky anomaly with and without DOS for $Sr_3Cr_2O_8$ (Figure 6). For the Gaussian DOS, we used the parameters $J_0 = 5.55\,\mathrm{meV}$ and $\delta = 3.5\,\mathrm{meV}$ determined by INS [3]. The original curve was evaluated with $\Delta = J_0$ (isolated dimers). Surprisingly, the curves are very similar to each other. The difference between them is maximal in the region of the maximum (2 %), and their maxima are only slightly shifted to each other. We compared our approximation with a more realistic DOS that is determined from a random phase approximation model for $Sr_3Cr_2O_8$ [24] (Figure 7). Nevertheless, also in this case the curves are very similar. Thus we decided not to consider the dispersion in our fits. This result suggests also that we do not obtain the energy gap Δ by fitting the experimental data. Therefore, we introduced a new quantity: the effective energy gap (Δ_{eff}). For sharp energy levels, it corresponds to the exchange constant, while for dispersive excitations $\Delta < \Delta_{\mathrm{eff}} < J_0$. Nevertheless, it may be a good approximation of J_0 in weakly interacting dimer systems (inset in Figure 6). The effective energy gap in the inset was obtained by setting $T_{\max} = 22.3\,\mathrm{K}$ (obtained from the green dashed line) in Equation (27).

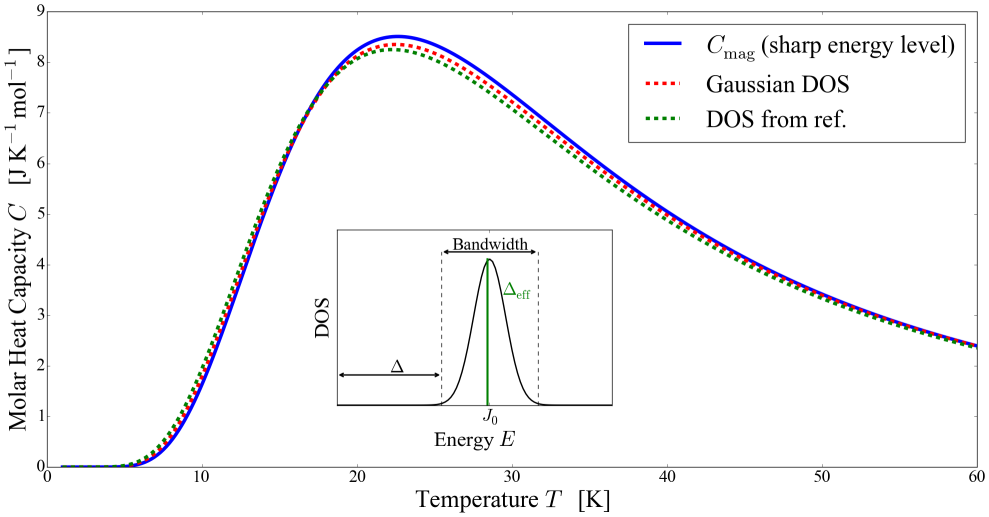

Figure 6: Schottky anomaly of the spin dimer system $Sr_3Cr_2O_8$ with both sharp (blue solid line) and dispersive excited state (red and green dashed line). For the Gaussian DOS, we used the exchange constant ($J_0 = 5.55\,\mathrm{meV}$) and the bandwidth ($\delta = 3.5\,\mathrm{meV}$) [3]. The green curve was obtained with the density of states in Figure 7. In the inset, the DOS of the red curve is shown and the relevant quantity are marked. The green line in the inset indicates the effective gap for the Schottky anomaly with the DOS from Ref. [24], $\Delta_{\mathrm{eff}} = 5.47\,\mathrm{meV}$.

2.4.2 Orbital Contribution to the Heat Capacity

Another example of Schottky anomaly is the orbital contribution to the heat capacity. In the compounds $Ba_3Cr_2O_8$ and $Sr_3Cr_2O_8$, the magnetic ions have a single electron in the fivefold degenerated $3d$ orbital. The tetrahedron crystal field splits the orbital into a higher lying threefold degenerated T_2 and a lower lying twofold degenerated E orbitals [25] (Figure 8). The last is formed by the $3z^2 - r^2$ and $x^2 - y^2$ orbitals. At the temperature T_{JT}, a Jahn-Teller transition occurs, changing the symmetry of the crystal from hexagonal into monoclinic with space group $C2/c$ [13, 6]. During the structural transition, the E orbital splits and the energy of $3r^2 - z^2$ decreases [13]. Consequently, the ground state ($3r^2 - z^2$) is separated from a non-degenerated excited state ($x^2 - y^2$) by an energy gap Δ_{oo}. The thermal excitations cause a Schottky-like peak in the heat capacity, which is described by the function

$$C_{\mathrm{oo}} = 2R(\beta\Delta_{\mathrm{oo}})^2 \frac{e^{-\beta\Delta_{\mathrm{oo}}}}{(1 + e^{-\beta\Delta_{\mathrm{oo}}})^2}, \tag{33}$$

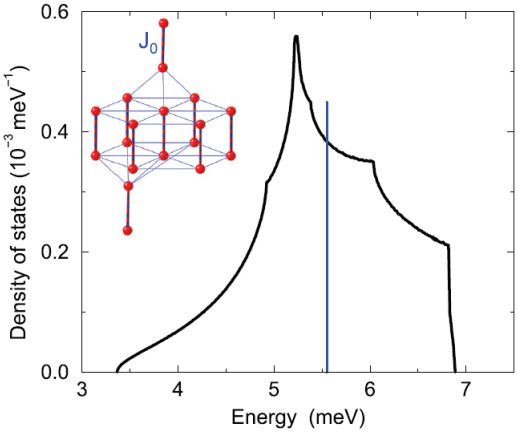

Figure 7: Density of state of $Sr_3Cr_2O_8$ as a function of the energy in the zero temperature limit. It is determined from a random phase approximation model [3]. The vertical line indicate the magnitude of the exchange constant $J_0 = 5.55\,\text{meV}$. Figure retrieved from Ref. [24]. The inset shows the dimer structure.

where the factor 2 arises from the number of Cr^{5+} ions per formula unit.

For temperatures higher than the transition temperature, the two orbitals have the same energy and no contribution to the heat capacity is observed. The transition temperature of $Sr_3Cr_2O_8$ was determined by powder neutron diffraction by Chapon *et al.* [13]. They observed several superlattice reflections for temperatures lower than $T_{JT} = 275\,\text{K}$, indicating a structural transition. A heat capacity measurement done by Wang *et al.* [17] shows a phase transition at $T_{JT} = 285\,\text{K}$, which they associated to the Jahn-Teller distortion. Kofu *et al.* determined by neutron diffraction that the transition temperature of $Ba_3Cr_2O_8$ is $T_{JT} = 70\,\text{K}$ [6]. This result was confirmed by Wang *et al.* [18] by a heat capacity measurement.

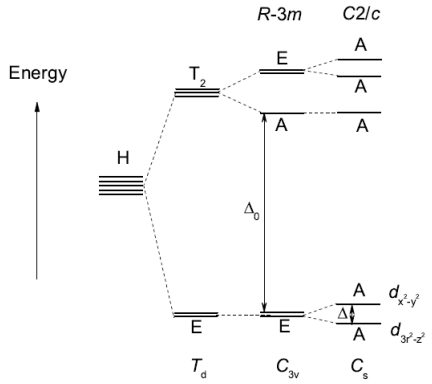

Figure 8: The $3d^1$ orbital of a Cr^{5+} ion. The degeneracy of the orbital is lifted by the tetragonal crystal field T_d, leading to the orbital triplet T_2 and doublet E states. The remaining degeneracies are lifted depending on the symmetry of the crystal structure. Figure retrieved from Ref. [25].

The orbital gap Δ_{oo} of $Ba_{3-x}Sr_xCr_2O_8$ is unknown, except for $x = 3$. Wang *et al.* [17] performed electron spin resonance (ESR) and estimated the energy gap to be $\Delta_{oo}(x = 3) = 33.4\,\text{meV}$. For the other value of x, we did the rough assumption $\Delta_{oo} \propto T_{JT}$, and used $\Delta_{oo}(3)$ to derive the orbital gap for the other x using the equation

$$\Delta_{oo}(x) = \frac{T_{JT}(x)}{T_{JT}(3)} \cdot \Delta_{oo}(3). \tag{34}$$

This value was then used as start parameter in our fit. The Jahn-Teller temperatures were determined by heat capacity (HC) measurements for $x = \{2.7,\ 2.8,\ 2.9,\ 3\}$ [26], and by neutron diffraction (ND) for $x = \{2.2,\ 2.8\}$ [27] (Figure 9). Moreover, values for $x = 0$ and $x = 3$ are known from previous publications [17, 18, 13, 6]. Unfortunately, the transition temperature for $x = 1.5$ was unknown. Therefore, we interpolated this temperature as follows. The transition temperature is not linear dependent on x, so we fitted the data in Figure 9 with two quadratic functions: one for the HC and one for the ND measurements. As start parameter for our fit, we chose the value obtained by interpolation between the value determined by HC measurements. At the end of the fitting procedure, we calculated back the Jahn-Teller temperature

using Equation (34). We retained the result as plausible, if the value of the Jahn-Teller temperature was in the yellow area (Figure 9). In order to verify the reliability of this method, we calculated the transition temperature for $x = 2.7$ from the result of the fit and compared this value with the experimental value of T_{JT}, which are in good agreement.

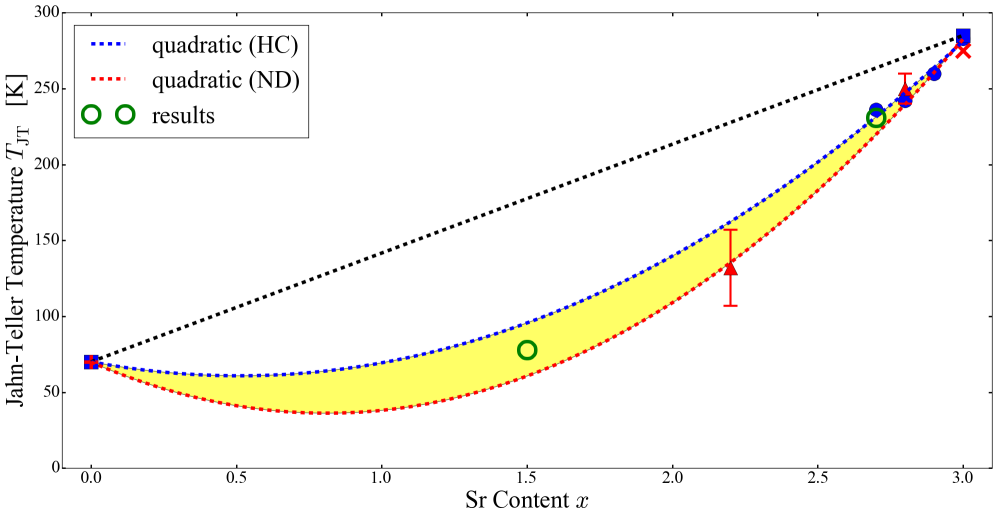

Figure 9: The Jahn-Teller transition temperature T_{JT} as a function of the Sr content x. The data points represented by red markers were measured by neutron diffraction (ND) [27, 13, 6], while the blue markers represent heat capacity (HC) measurements [26, 17, 18]. The blue and red dashed lines are two fits that may predict the behaviour of T_{JT} for different values of x. The yellow area delimit the region of believability for the transition temperature. The green circle are the temperatures obtained with Equation (34), using the result of the fits (Δ_{oo}).

3 Experimental Techniques

3.1 Sample Preparation

The samples of $Ba_{3-x}Sr_xCr_2O_8$ (for $x = \{0, 0.3, 0.6, 0.9, 1.2, 1.5, 1.8, 2.7, 3\}$) were prepared at the University of Zurich using $BaCO_3$, $SrCO_3$ and CrO_3 as reactants. The solid reaction

$$(3-x)BaCO_3 + xSrCO_3 + CrO_3 + O_2 \longrightarrow Ba_{3-x}Sr_xCr_2O_8 + 3CO_2 \tag{35}$$

occurred in a high temperature furnace. The reactants were mixed, pressed and heated at 1250 °C for 24 h. The reaction was then quenched with liquid nitrogen. The resulting material was grounded, pressed and then heated again under the same conditions. The last procedure was repeated three times. Two compounds ($x = 0$ and $x = 0.3$) were melted and stuck together with the Al_2O_3 sample holder. Therefore, we chose a lower temperature (1000 °C) for the last step of the preparation. The samples were dark grey. Some samples showed dark green color shades in the internal part. A similar result was obtained by H. Grundmann [7]. The consistency of the pills was hard at the beginning, but some samples became friable (or powdery) after a while. We were not able to explain this phenomenon, since the x-ray diffraction analysis did not show significant changes in the crystal structure. Because of time restriction, we used only the samples $x = \{0, 1.5, 2.7, 3\}$ for the heat capacity measurements.

Afterwards, we performed further heat capacity measurements of polycrystalline samples of $Sr_3Cr_2O_8$ and $Ba_3Cr_2O_8$ prepared by H. Grundmann. In particular, we wanted to compare the data quality of the two different preparation methods. The samples were grown with an optical floating zone method to obtain single crystals (details about the procedure are reported in his doctoral dissertation [7]). However, they turned out to be high quality polycrystalline samples.

In this thesis, the magnetic dependence of the Schottky anomaly of $Ba_{0.1}Sr_{2.9}Cr_2O_8$ was analysed as well. The sample, which was a single crystal, had been prepared by A. Gazizulina [26]. The powder preparation is similar to the first method explained in this chapter, and the single crystal growth was performed in the Crystal Laboratory at the Helmholtz Zentrum Berlin für Materialien und Energie (HZB), Germany, using a high temperature optical floating zone furnace (FZ-T-10000-H-VI-VPO).

3.2 X-Ray Powder Diffraction

In order to verify the purity and to determine the lattice parameters of $Ba_{3-x}Sr_xCr_2O_8$, a small amount of the samples were used for XRD measurements. Powder x-ray diffraction data were collected using the *Stoe* IPDS at the University of Zurich equipped with monochromatic CuKα radiation ($\lambda = 1.5406$ Å). The step size of the angle was set to 0.015° and the measurements were performed over the 2Θ range 5°-95°. The time of radiation was set to 150 seconds. The *Stoe* IPDS operates in transmission mode (Figure 10). The sample was grounded and distributed between two Scotch tapes. The sample holder was rotated during the measurement to avoid secondary effects due to inhomogeneous distribution of the powder. This XRD diffractometer provides good accuracy of the peak positions [7]. Consequently, the lattice parameters can be estimated with high precision. However, the x-ray photons are subject to inelastic scattering and absorption when they pass through the plastic layers and the sample powder, as reported by Grundmann [7]. These effects reduce the precision of the atomic coordinate determination.

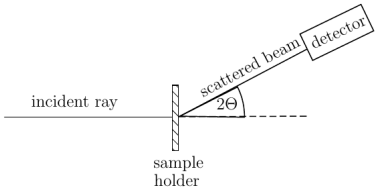

Figure 10: Sketch of the transmission mode (Debye-Scherrer diffraction geometry).

3.3 Relaxation Calorimetry

The relaxation calorimetry is one of the various techniques for the measurement of the heat capacity. This procedure is based on the evaluation of the relaxation time constant (τ), which describes the time needed for a system A to decrease its temperature by a factor e (natural number) when it is in thermal contact

with a system B ($T_A > T_B$). More specifically, the sample and the platform are initially in thermal equilibrium with a thermal bath (temperature T_{Tb}). A heating device applies a constant power P_0 to the platform, increasing its temperature and the temperature of the sample by ΔT. Then the device is turned off and the sample's temperature $T_S(t)$ decreases exponentially, going back to the thermal equilibrium with the thermal bath. The relaxation time τ is fitted and the heat capacity is calculated according to the equation

$$C = \kappa\tau, \tag{36}$$

where κ is the thermal conductance of the thin wires that connect the platform to the thermal bath [28]. Assuming a good conductance between the sample and the platform, the time progression of the temperature can be approximated by

$$T_S(t) - T_{Tb} = \Delta T \cdot e^{-t\kappa/(C_S+C_{SH})} = \Delta T \cdot e^{-t/\tau}, \tag{37}$$

where C_S and C_{SH} are the heat capacity of the sample (S) and sample holder (SH) respectively. The temperature difference ΔT must be small, so that τ can be considered as a constant. Figure 11 shows the sample temperature as a function of the time. The temperature of the thermal bath is then varied in order to collect a set of data points

$$C(T) = C_S + C_{SH}. \tag{38}$$

A measurement cycle of the heat capacity consists of two parts: an addenda measurement and a sample measurement. In the first part, the heat capacity of the sample holder C_{SH} is measured. In the second part, the total heat capacity $C_S + C_{SH}$ is measured, and the addenda measurement is subtracted from it, giving the sample's heat capacity C_S.

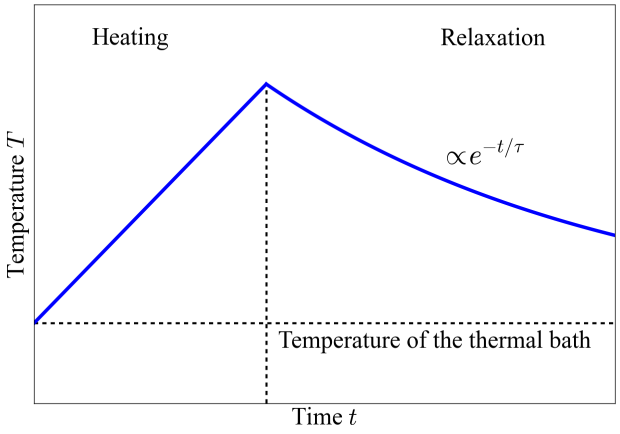

Figure 11: Time progression of the sample temperature. Initially, the temperature is increased by a constant supply of heat. Then the heater is turned off and the temperature decreases exponentially.

The heat capacity measurements were performed at the University of Zurich using a Physical Property Measurement System (Quantum Design). The PPMS is a relaxation calorimetry and measures the heat capacity at constant pressure

$$C_P = \left.\frac{\partial Q}{\partial T}\right|_P. \tag{39}$$

According to the user's manual [29], in a fixed time interval a heater positioned under the sample platform applies a known amount of heat while a thermometer monitors the temperature (Figure 12). The temperature decrease is fitted taking into account also the thermal resistance between the sample and the holder. The temperature relaxation is then described by two time constants, τ_1 and τ_2, leading to precise results also in the case of bad conduction between the sample and the holder.

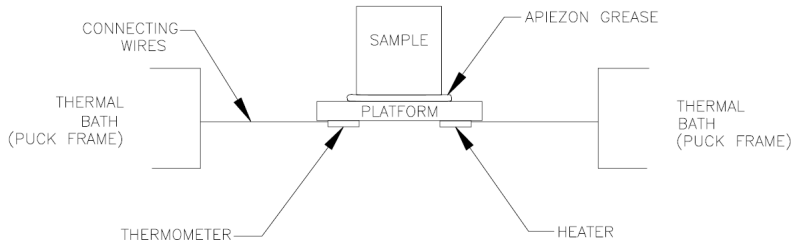

Figure 12: Thermal connections between the sample and sample platform in the PPMS heat capacity option. Picture retrieved from the PPMS Heat Capacity Option Users's Manual.

4 Measurements

4.1 X-Ray Measurements

In order to verify the results of the sample preparation, we performed several XRD experiments. The intensity peak positions are affected by the values of the lattice parameters ($a = b$ and c), consequently they are shifted for different Sr content x. For each sample, one peak of the intensity pattern was fitted with a Pseudo-Voigt function, obtaining a qualitative representation of this effect (Figure 13).

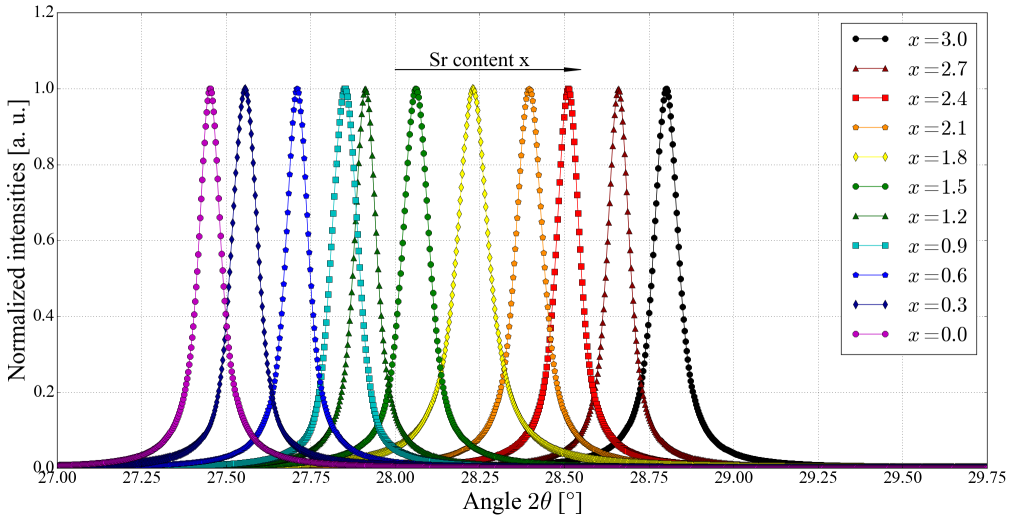

Figure 13: Normalized intensity peaks (0,1,5) fitted from XRD data as a function of the 2Θ angle. The peaks shift to the right with increasing Sr content (x).

The x-ray data were analysed using the Rietveld method in FullProf. All intensity peaks were described by the hexagonal space group $R\bar{3}m$ (Figures 32, 36, 39, 42, in Appendix). Because of the poor sensitivity of the XRD pattern on the atom's coordinates (particularly for the oxygen atoms), we extrapolated only the lattice parameters from the fit of the intensity pattern, without considering the atomic coordinates. We represented the lattice parameters as a function of the Sr content x and proved the linear dependence predicted by the Vegard's law (Figure 14). The lattice parameters are very similar to the results of a neutron diffraction experiment that was performed on similar samples [7]. Based on these results, we assessed that our samples were adequate for further analyses. Next, we performed the heat capacity measurements.

4.2 Heat Capacity Measurement

4.2.1 Molar Heat Capacity of $Sr_3Cr_2O_8$

We measured the heat capacity of both the polycrystalline sample prepared at the University of Zurich (mass: 8.0 mg , we refer to this sample using the letter (M)) and the sample prepared by Grundmann (mass: 5.9 mg, we refer to this sample using the letter (G)). Plotting $C_M - C_G$ on a logarithmic scale (Figure 33, in Appendix), we observe a constant difference (0.0467) between the experimental data in the temperature range $40 - 150\,\mathrm{K}$. Therefore, we divided the data (M) by the factor $e^{0.0467} = 1.048$ to obtain a better match between the data. This factor can arise from an inaccurate measurement of the mass, or, as in the case of $x = 0$, from a small loss of material when the sample was placed on the sample holder, since the sample was powdery and fragile. The two sets of data coincide over the full range of temperatures, except below 7 K. Here, the sample (M) exhibits a larger contribution to the heat capacity than the sample (G) (Figure 34, in Appendix). We attributed this contribution to the impurities of the sample, which are more abundant in the sample (M) than in (G), because of the preparation method. The theoretical curve for this compound was proposed by Wang *et al.* [17]. It takes into account the three components mentioned in Chapter 2.2: lattice, orbital and magnetic contributions. The model matches well to the data at low temperatures, while it slightly deviates from the data at high temperatures (differences of about $2 - 5\,\%$). For the magnetic contribution, we used the function

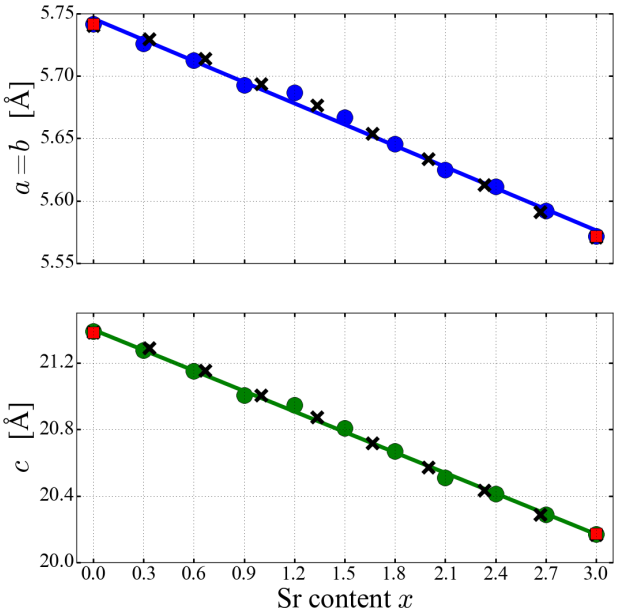

Figure 14: Lattice parameters of $Ba_{3-x}Sr_xCr_2O_8$ as a function of the Sr content x (dots) estimated by XRD. A comparison between our results and the values obtained from neutron diffraction experiments [7] (black crosses) and from XRD [1, 2] (red squares) is shown.

defined by Equation (25), while at the origin, Wang *et al.* used a function that describes a three-level system. They performed ESR to estimate the singlet-triplet excitations (5.13 meV and 6.08 meV) and used these energies (with degeneracy $g_1 = 2$ and $g_2 = 1$) for the theoretical curve. However, the result is very similar to the Schottky anomaly obtained using $J_0 = 5.55$ meV (determined by INS [3]) as an energy gap (Figure 35, in Appendix), and both describe almost well the experimental data. Nevertheless, both the lattice and magnetic contributions needed to be slightly adapted, so we fitted the data (Figure 15). The resulting characteristic temperatures for both samples are similar to the original model. Only the Einstein temperature E_3 is markedly changed, but this factor cannot affects the shape of the Schottky anomaly. For the sample (G), the effective energy gap is $\Delta_{\text{eff}} = (5.42 \pm 0.05)$ meV and the fraction of dimerized ions is $n_d = 1$, as observed by Grundmann in the magnetisation measurement. For the other sample, $Sr_3Cr_2O_8$ (M), the gap is $\Delta_{\text{eff}} = (5.50 \pm 0.08)$ meV and $n_d = 0.98 \pm 0.02$, in good agreement with the previous result.

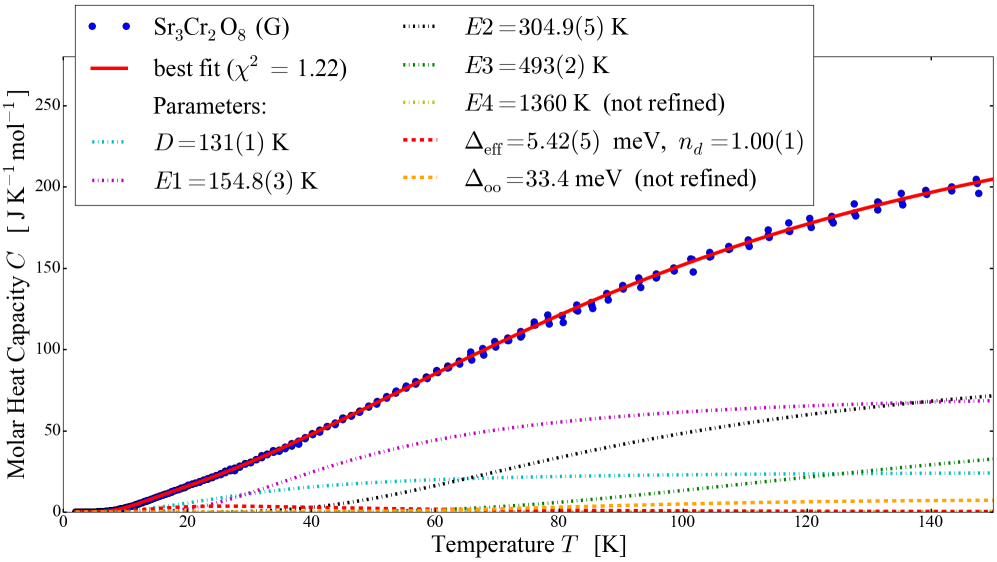

Figure 15: Molar heat capacity C of $Sr_3Cr_2O_8$ (G) as a function of the temperature T (blue dots). The red solid line represents the best fit. The fit parameters are reported in the legend. The orbital energy gap was fixed at $\Delta = 33.4$ meV.

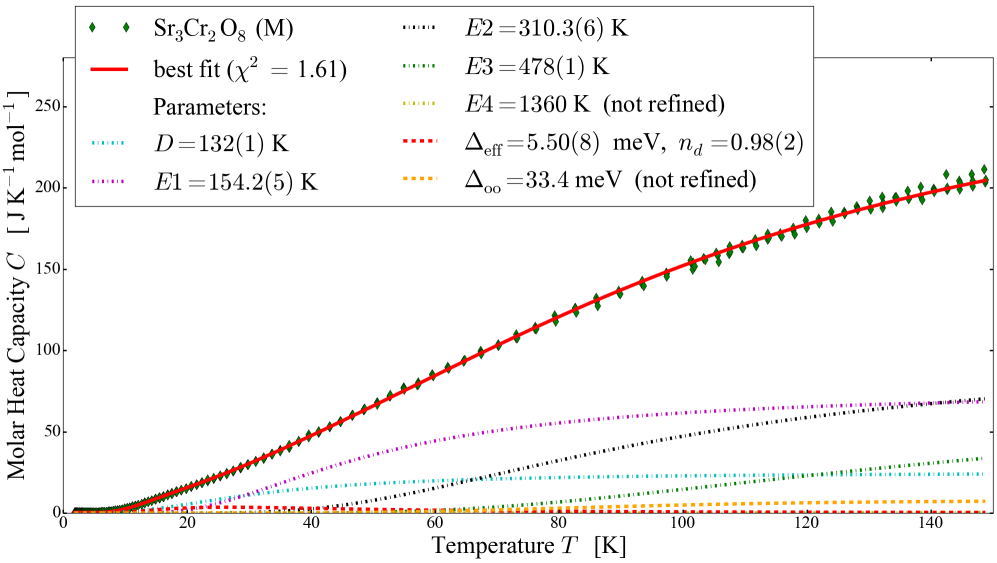

Figure 16: Molar heat capacity C of $Sr_3Cr_2O_8$ (M) as a function of the temperature T (green diamonds). The red solid line represents the best fit. The fit parameters are reported in the legend. The orbital energy gap was fixed at $\Delta = 33.4$ meV.

Figure 17 shows the heat capacity (G) after subtraction of the lattice and orbital contributions, and its best fit. The data show an anomalous tail at low temperatures, which we fitted with Equation (23) for a two-level system ($C_{\rm imp}$). Interestingly, we found an analogous contribution also in the other compounds. Probably, this contribution is due to impurities. In fact, the residual heat capacity ($C - C_{\rm latt} - C_{\rm oo}$) of $Sr_3Cr_2O_8$ (M) shows a more prominent tail than the homonym sample (G) (Figure 18). In this case, the additional contribution was fitted by the sum of two Schottky anomaly, instead of a single function. The energy gap used in $C_{\rm imp}$ for $Sr_3Cr_2O_8$ (G) has similar magnitude as that used to describe $C_{\rm imp,1}$ for (M). It could be that the samples have one common impurity contribution. The factor N_i is larger for the polycrystalline sample (M), supporting the assumption of the impurities as a cause of the additional contributions. Indeed, the quality of the sample (G) is expected to be higher than that of (M).

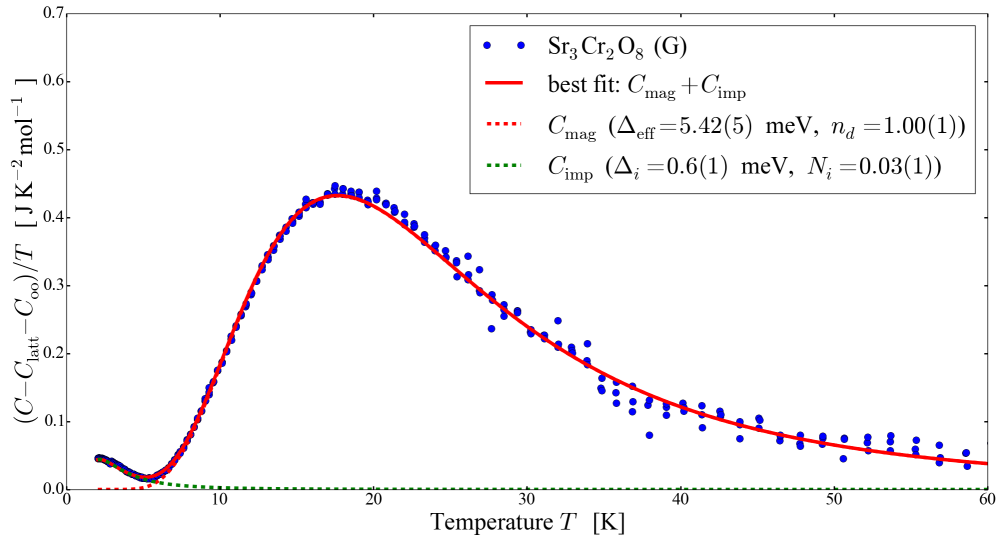

Figure 17: Residual heat capacity $(C - C_{\rm latt} - C_{\rm oo})/T$ as a function of the temperature T (blue dots). The theoretical curve was obtained by the sum of the magnetic and the impurities contributions (the parameters are reported in the legend).

4.2.2 Molar Heat Capacity of $Ba_{0.3}Sr_{2.7}Cr_2O_8$

We measured the molar heat capacity of a $Ba_{0.3}Sr_{2.7}Cr_2O_8$ sample with mass 6.9 mg. In a first step, we compared the data with a theoretical curve, obtained from the interpolation method reported in

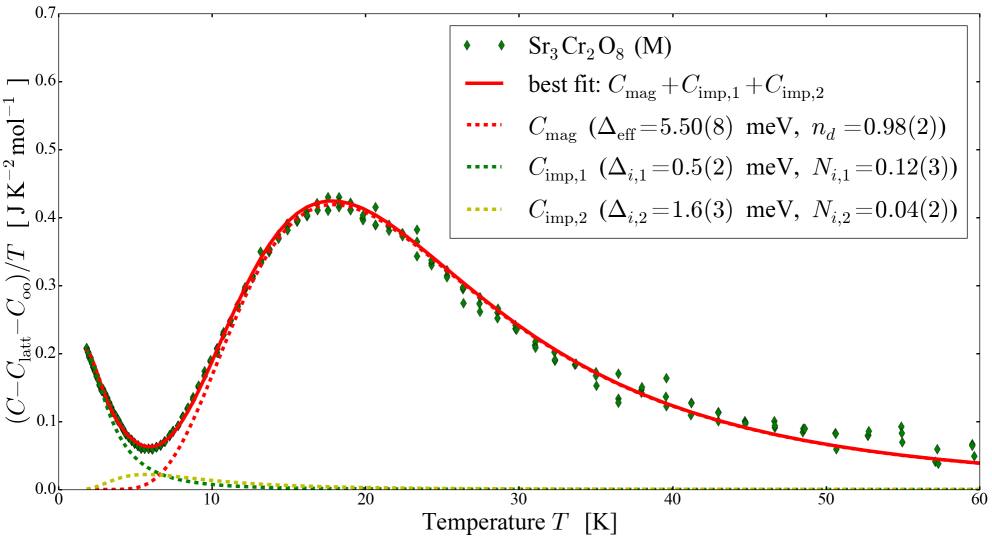

Figure 18: Molar heat capacity $C - C_{\text{latt}} - C_{\text{oo}}$ divided by the temperature T as a function of the temperature (green diamonds). The theoretical curve was obtained by the sum of the spin dimer and two additional (C_{imp}) contributions (the parameters are reported in the legend).

Chapter 2.3.3 (Figure 37, in Appendix). This method overestimates the molar heat capacity, in particular at high temperatures. However, subtracting this theoretical curve, we noted that the Schottky anomaly had the expected shape, indicating that the model matches well to the data (Figure 38, in Appendix). From the position of the maximum, we estimated the effective gap $\Delta_{\text{eff}} = 4.85\,\text{meV}$, using Equation (27).

We fitted the data as in the previous case, taking into account the three discussed contributions and two additional contributions due to impurities. As the starting fit parameters of the lattice model, we used the values obtained from the interpolation method, Equation (16). For the orbital gap Δ_{oo}, we assumed $\Delta_{oo} \propto T_{JT}$, as reported in Chapter 2.4.2. The temperature of Jahn-Teller distortion ($T_{\text{JT}} = 236\,\text{K}$) is known from measurements of Gazizulina at the University of Zurich. Figure 19 shows the result of the fit. As expected, the characteristic temperatures D and E_1 decrease with increasing mass and unit cell volume, whereas E_2 and E_3 increased. We focused our interest on the low temperature range, thus on D and E_1, since the other characteristic temperatures do not affect the Schottky anomaly. The ratio between the Debye temperatures of $x = 3$ and $x = 2.7$ is 0.97, while the ratio between the Einstein temperatures is 0.98. These results are consistent with the scaling factor in Equation (16). The resulting orbital gap agrees with the experimental data, as shown in Figure 9. The effective gap is $\Delta_{\text{eff}} = (4.91 \pm 0.06)\,\text{meV}$ that is similar to the value estimated before. The factor n_d is smaller than in $Sr_3Cr_2O_8$, suggesting the presence of a large amount of free Cr^{5+} ions (i. e. not dimerized ions). This could be related to the mixing of Ba and Sr ions, since n_d is further reduced in $x = 1.5$.

The residual heat capacity ($C - C_{\text{latt}} - C_{\text{oo}}$) was fitted by the sum of a magnetic and two additional terms (2-level system) due to impurities (Figure 20). Using the same energy gaps $\Delta_{i,1,2}$ as for $Sr_3Cr_2O_8$ (M), we obtained a good match to the data.

4.2.3 Molar Heat Capacity of $Ba_{1.5}Sr_{1.5}Cr_2O_8$

We measured the molar heat capacity of a $Ba_{1.5}Sr_{1.5}Cr_2O_8$ sample (6.8 mg). As for $x = 2.7$, we compared the data with the theoretical curve obtained by the interpolation between the known heat capacity of the parent compounds (Figure 44, in Appendix). At high temperatures, the model well describes the experimental data. At low temperatures, the Schottky anomaly is markedly reduced, in fact, it appears like a light deviation from the theoretical model. Analysing the residual heat capacity (Figure 41, in Appendix), we estimate a reduction of the Schottky anomaly of 40 % from the height of the peak, while the impurity contributions are much larger than in the other compounds. The fit was performed with the same method as in the previous cases (Figure 21). The resulting Debye temperature is smaller than that of $x = 3$. The ration $D(x = 1.5) : D(x = 3)$ is consistent with the scaling factor in Equation (16). In contrast with our expectation, E_1 increases. We interpret this result as a signal that our assumptions about the orbital contribution (Chapter 2.4.2) may do not reflect well the real behaviour of the orbital gap. In fact, reducing the orbital contribution, the temperature E_1 decreases. This can be related to a

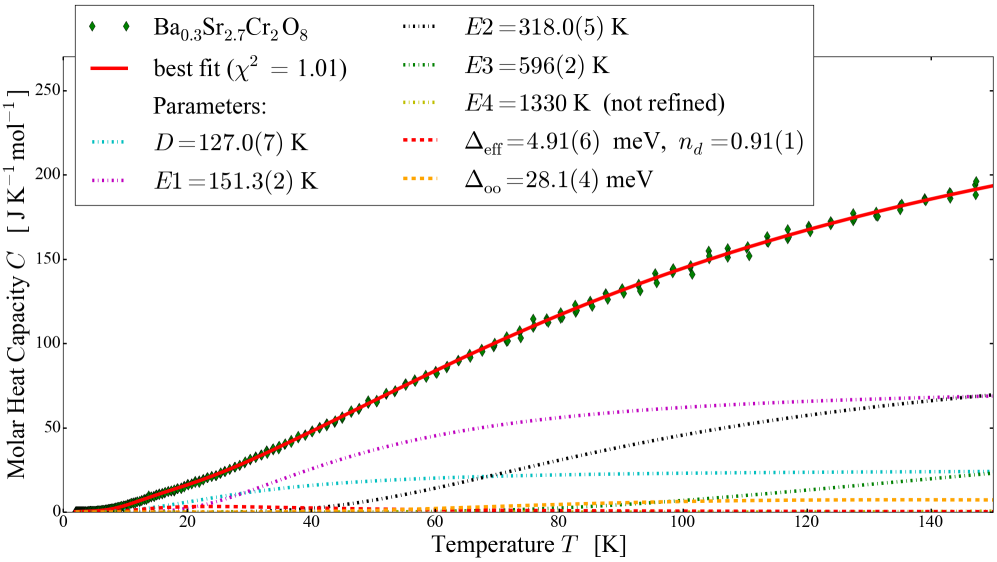

Figure 19: Molar heat capacity C of $Ba_{0.3}Sr_{2.7}Cr_2O_8$ as a function of the temperature T (green diamonds). The red solid line represents the best fit. The parameters of the fit are reported in the legend.

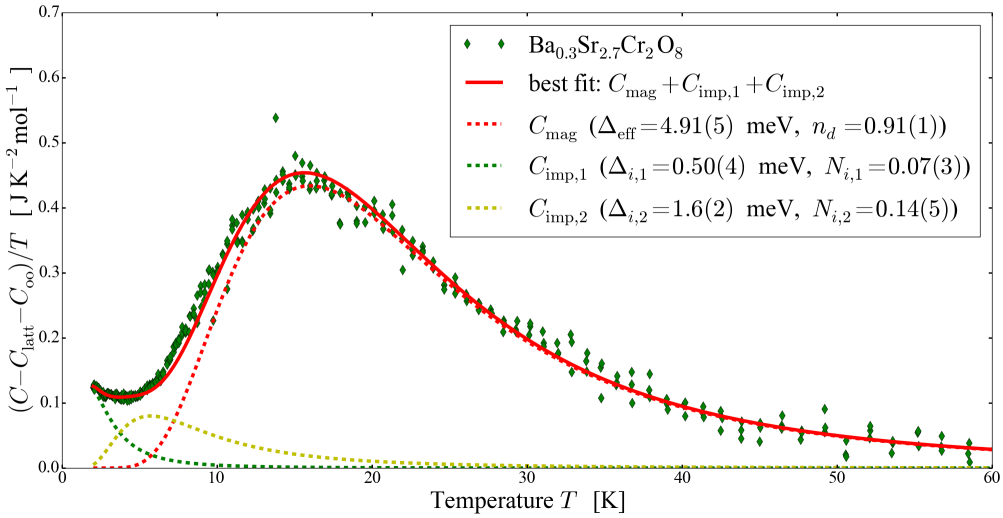

Figure 20: Residual heat capacity $(C - C_{\rm latt} - C_{\rm oo})/T$ of $Ba_{0.3}Sr_{2.7}Cr_2O_8$ as a function of the temperature T. The theoretical curve (red solid line) is composed by three terms: the magnetic ($C_{\rm mag}$) and the impurity ($C_{\rm imp1,2}$) contributions. The single contributions are shown with dashed lines.

partial suppression of the Jahn-Teller distortion reported by Grundmann *et al.* [14]. In addition, the structural transition is not visible in the heat capacity, supporting this hypothesis. The effective energy gap for this compound is $\Delta_{\text{eff}} = (4.1 \pm 0.1)$ meV. The uncertainty of the result is larger than compared to the other gaps, because the contribution of the impurities to the heat capacity is important. The reason may be related to local disorder due to the mixing of Sr and Ba atoms. The resulting n_d agrees with the fraction reported in a magnetisation measurement [7] (Figure 4).

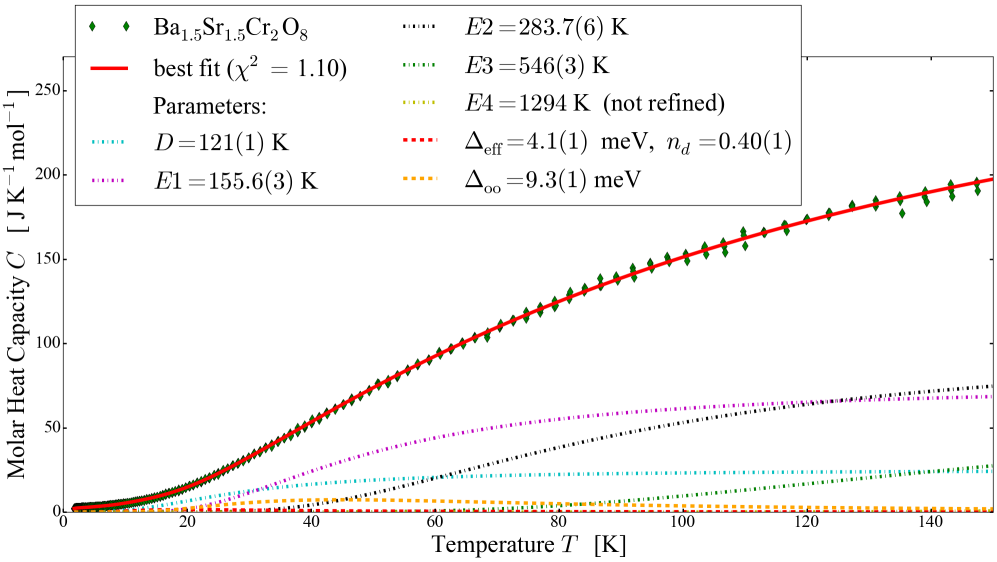

Figure 21: Molar heat capacity C of $Ba_{1.5}Sr_{1.5}Cr_2O_8$ as a function of the temperature T (green diamonds). The red line represent the fit. The fitting parameters are reported in the legend.

The residual heat capacity $(C - C_{\text{latt}} - C_{\text{oo}})$ appears like a broad peak (Figure 22, inset), which is broader and smaller than in the other compounds. The data were fitted again by the sum of a magnetic and two impurity contributions. The energy gaps of the two-level systems were in the same range as for $x = 3$ and $x = 2.7$. The result of the fits suggest the presence of two level system common in all compounds $Ba_{3-x}Sr_xCr_2O_8$ prepared with the same method, namely solid solution reported in Chapter 3.1. In fact, the impurity contribution to the heat capacity of our samples (denoted with (M) and represented by green diamonds) can be fitted by two terms, except for $x = 0$. In contrast, in the samples prepared by Grundmann (denoted with (G)) this contribution is fitted by a single Schottky anomaly.

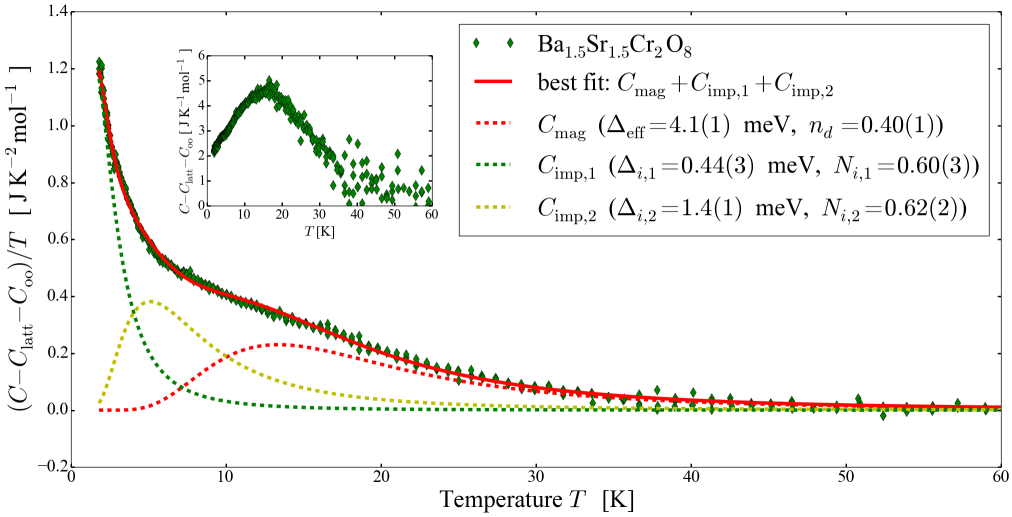

Figure 22: Residual heat capacity $(C - C_{\text{latt}} - C_{\text{oo}})/T$ as a function of the temperature T (green diamonds). The theoretical curve (red solid line) is a sum of magnetic and impurity contributions. The dashed lines represent the single terms of the model. In the inset, the residual heat capacity $C - C_{\text{latt}} - C_{\text{oo}}$ is represented a s a function of the temperature.

4.2.4 Molar Heat Capacity of $Ba_3Cr_2O_8$

As in the case of $Sr_3Cr_2O_8$, we measured the molar heat capacity of both the samples $Ba_3Cr_2O_8$ (M) (mass: 8.1 mg) and $Ba_3Cr_2O_8$ (G) (mass: 3.2 mg). The heat capacity of the sample (M) was markedly smaller than that of the sample (G). Because the sample was friable, we suspect that the sample lost a small amount of material during the displacement from the balance to the sample holder. Therefore, the experimental data (M) were multiplied by the factor 1.176, which was obtained in the same way as for $Sr_3Cr_2O_8$ (Figure 43, in Appendix). We plotted the molar heat capacity of (M) and (G) in the same graphic to compare the quality of the measurement (Figure 44, in Appendix). Surprisingly, the curves have slightly different shapes. With regards to the experimental data of $Ba_3Cr_2O_8$ (G), we observed a phase transition at the temperature of $T_{\mathrm{JT}} = (69 \pm 1)\,\mathrm{K}$, in agreement with the value reported in previous publications (70 K) [6, 18]. On the other hand, the heat capacity of $Ba_3Cr_2O_8$ (M) does not show the structural transition. The theoretical model in Figure 44 takes into account three contributions: the lattice term (proposed by Wang *et al.*), the orbital term (Chapter 2.4.2) and the Schottky anomaly with $\Delta_{\mathrm{eff}} = J_0 = 2.38\,\mathrm{meV}$ (interaction constant determined by INS [6]). It describes well the data, especially for low temperatures, while it deviates from the data in the region of the transition temperature T_{JT}. Comparing the Schottky anomaly of the two samples (Figure 45, in Appendix), we noted that the peaks have some differences, in particular, the peak heights and positions do not coincide. The sample (G) is more pronounced and the position of the maximum remind to the gap 2.2 meV, while the sample (M) is well described by the Schottky anomaly with $\Delta_{\mathrm{eff}} = J_0 = 2.38\,\mathrm{meV}$. The difference between the peaks can be explained by the presence of different amount of impurities. In contrast with the case of $x = 3$, it seems that the sample (M) has less impurities than the sample (G).

We fitted the data and obtained two different sets of characteristic temperatures. As expected, the Debye temperatures of both samples are smaller than that of the other x values, and again, they are compatible with the scaling factor in Equation (16). In contrast, the Einstein temperatures E_1, E_2 and E_3 are observably different. The reason of this discrepancy could be the strange oscillations observed in the heat capacity of $Ba_3Cr_2O_8$ (M), and of course the different shape of the curves. The non-physical oscillations are present particularly at high temperatures. Moreover, they have a constant period of 10 K between $80 - 110\,\mathrm{K}$ (marked with arrows in Figure 16). We attribute this to some problems in reaching and maintaining high vacuum in the PPMS. This problem may cause the small change of the shape of the heat capacity and hide the structural transition.

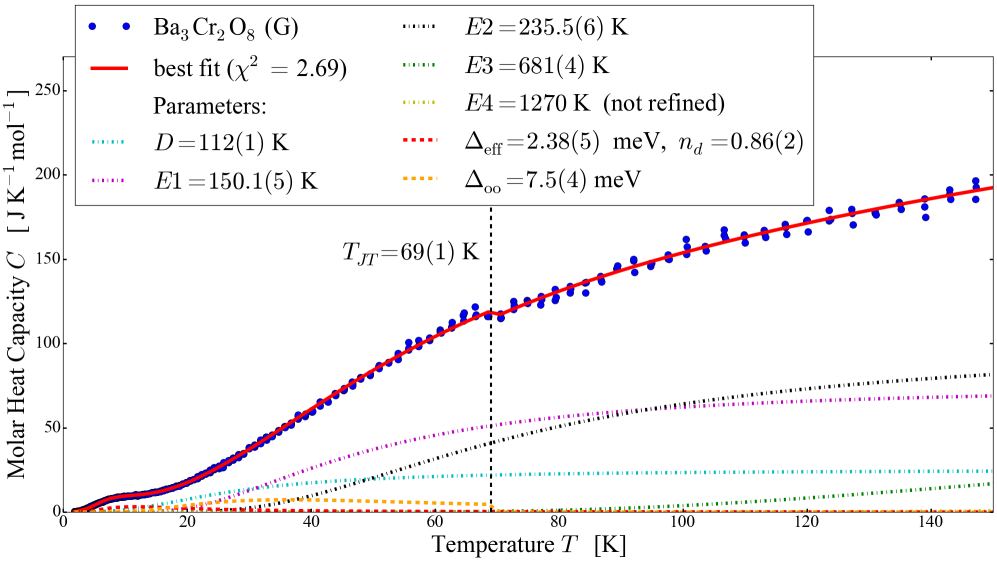

Figure 23: Experimental data of the molar heat capacity C of $Ba_3Cr_2O_8$ (G) as a function of the temperature T (blue dots). The red solid line represents the fit. The fitting parameters are reported in the legend.

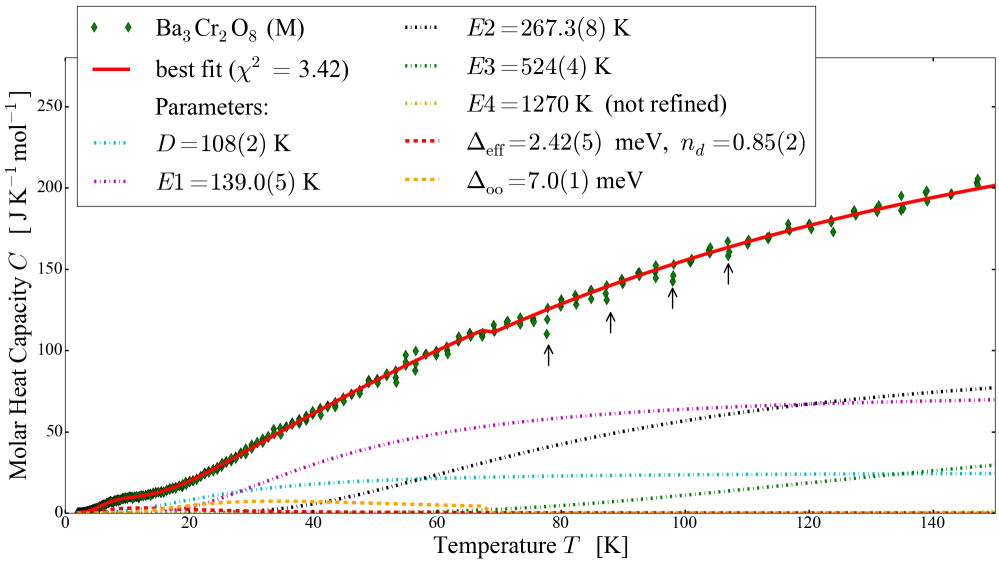

Figure 24: Experimental data of the molar heat capacity C of $Ba_3Cr_2O_8$ (M) as a function of the temperature T (green diamonds). The red solid line represents the fit. The fitting parameters are reported in the legend. The arrows indicate the strange oscillation of the heat capacity.

After subtraction of the lattice and orbital contributions, we fitted the residual heat capacity with the sum of the magnetic (C_{mag}) and the impurity (C_{imp}) contributions (Figures 25 and 26). Despite the visible differences between the two peaks of the residual heat capacity, the magnetic contributions are very similar (Figures 25, 26). The effective gap is $\Delta_{\mathrm{eff}} = (2.38 \pm 0.05)\,\mathrm{meV}$ for the sample (G), and $\Delta_{\mathrm{eff}} = (2.42 \pm 0.05)\,\mathrm{meV}$ for (M). In addition, the fraction of dimerized ions is almost the same for both samples. The energy gap related to the impurities is in the same range of energies for both samples ($0.8 - 0.9\,\mathrm{meV}$). The impurity contribution is larger in the sample (G) than in (M), which is in contrast with the result for $x = 3$.

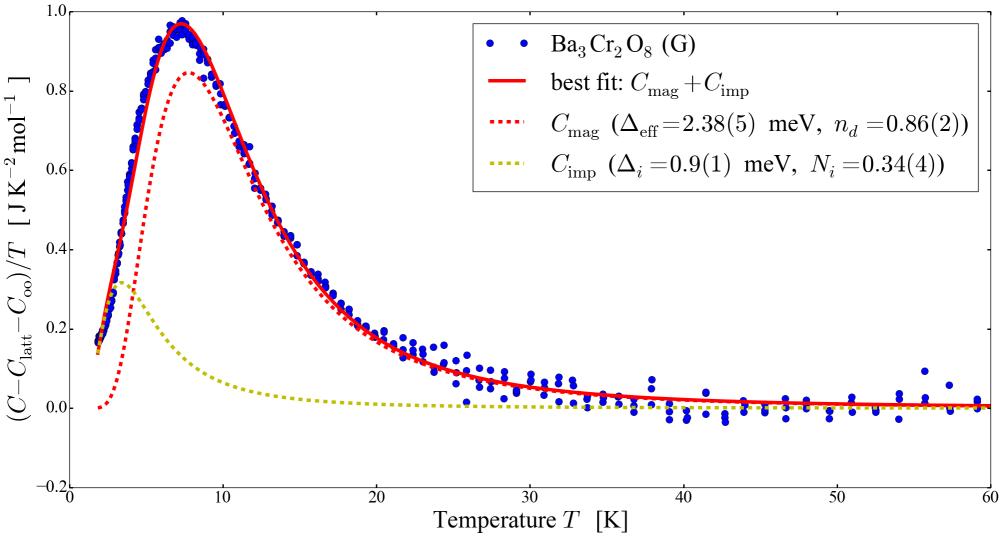

Figure 25: Residual heat capacity $(C - C_{\mathrm{latt}} - C_{\mathrm{oo}})/T$ as a function of the temperature T (blue dots). The theoretical curves (red solid line) is given by the sum of two contributions: $C_{\mathrm{mag}} + C_{\mathrm{imp}}$. The dashed lines represent the single terms of the theoretical model.

4.3 Magnetic Dependence of the Heat Capacity

The theoretical model of the heat capacity is complex and the fitting parameters are sometimes strongly correlated to each other. This is especially the case for the characteristic temperatures D and $E1$ with the

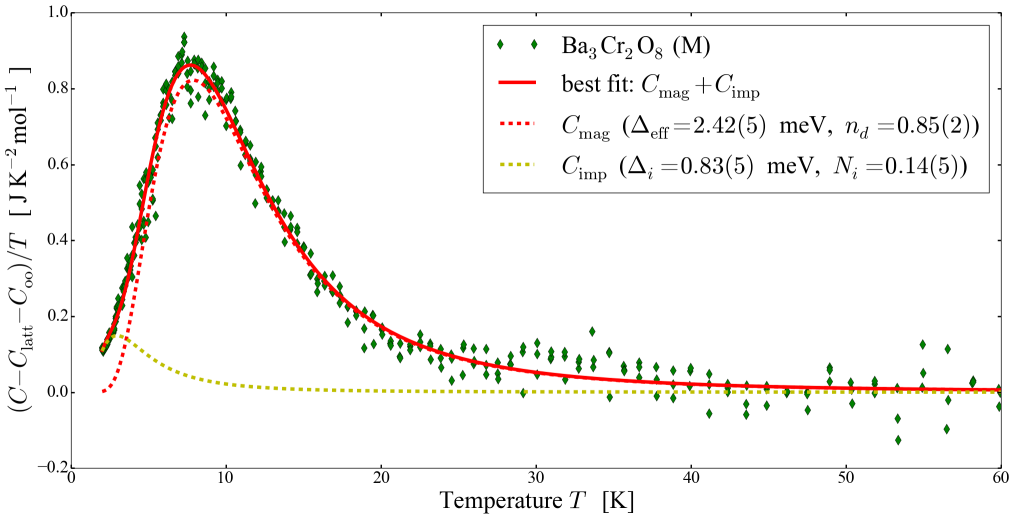

Figure 26: Residual heat capacity $(C - C_{\text{latt}} - C_{\text{oo}})/T$ as a function of the temperature T (blue dots). The theoretical curves (red solid line) is given by the sum of two contributions: $C_{\text{mag}} + C_{\text{imp}}$. The dashed lines represent the single terms of the theoretical model.

energy gap Δ. As a consequence, the subtraction of the lattice contribution could affect the shape and the position of the magnetic Schottky anomaly. Furthermore, the orbital gap is unknown for intermediate amounts of Sr ($0 < x < 3$), making it hard to fit the experimental data without further analyses. All these problems could be theoretically avoided by performing an additional heat capacity measurement with an external magnetic field ($C(T, H)$). The difference $\Delta C = C(T, H) - C(T, H = 0)$ corresponds to ΔC_{mag}, since the lattice and orbital contributions are independent from the magnetic field. So, one needs to consider a theoretical model that takes into account only the magnetic contribution.

We did not perform such measurements because of time restriction, but we analysed heat capacity data of $x = 2.9$, which were measured at the Laboratoire National des Champ Magnétiques Intenses (LNCMI), Grenoble. The measurements were performed up to the magnetic field $H = 19\,\text{T}$. The experimental data were measured in different temperature ranges and with different steps and we therefore used a spline interpolation to obtain a function that represents well the data $C(T, 0)$. This function was subtracted from the data $C(T, H)$ to obtain ΔC (Figure 27). Unfortunately, most of the experimental data were evaluated in the restricted temperature range $2 - 15\,\text{K}$, while we need to consider the range of temperatures $2 - 50\,\text{K}$ to observe the entire Schottky anomaly (inset in Figure 28). In this small range of temperatures, the data show a quasi symmetric peak, which is centred at about 8.5 K and becomes more pronounced for increasing magnetic field values.

The theoretical curves are given by $\Delta C_{\text{mag}} = C_{\text{mag}}(T, H) - C_{\text{mag}}(T, 0)$, where C_{mag} is given by the Equation (23) with the energy states $\varepsilon_{0,1,2,3} = \{0,\ \Delta_{\text{eff}} - g\mu_{\text{B}}H,\ \Delta_{\text{eff}},\ \Delta_{\text{eff}} + g\mu_{\text{B}}H\}$. The g-factor is $g = 1.94$ for both $Sr_3Cr_2O_8$ and $Ba_3Cr_2O_8$, as determined by high field ESR [30]. This value was confirmed by electron paramagnetic resonance for $Sr_3Cr_2O_8$ [12], and by other ESR experiments for $Ba_3Cr_2O_8$ [32, 31]. The effective gap Δ_{eff} is thus the unique fitting parameter in this model. However, we realized that the experimental data cannot be fitted using only the gap as free parameter.

In order to compare the experimental data with plausible theoretical curves, we estimated the effective gap from the residual heat capacity ($H = 0$) and obtained $\Delta_{\text{eff}} \approx 5.2\,\text{meV}$. Then, we plotted the result for all magnetic fields (Figure 28). The curves have a maximum in the range of temperatures $2 - 15\,\text{K}$ similar to the experimental data. However, the peak in the theoretical curves are centered at about 9.5 K and their height is larger than that of the experimental data. In addition, the data get in the negative plane at low temperatures, indicating that there is another magnetic field dependent component, which has to be taken into account.

To better understand the discrepancy between experimental data and theoretical model, we fitted the data ($H = 0$). This data were collected in the range of temperatures $2 - 25\,\text{K}$. Here, the relevant lattice contributions are the Debye (D) and the Einsten (E_1) terms, thus $C_{\text{latt}} = D + 3E_1$. From the fit we obtained $\Theta_{\text{D}} = (131 \pm 1)\,\text{K}$ and $\Theta_{\text{E1}} = (153.7 \pm 0.1)\,\text{K}$, in agreement with Equation (16). The orbital contribution was omitted in the theoretical model, because it is not relevant at low temperatures. The residual heat capacity ($C - C_{\text{latt}}$) was fitted by the sum of the magnetic contribution (C_{mag}) and two

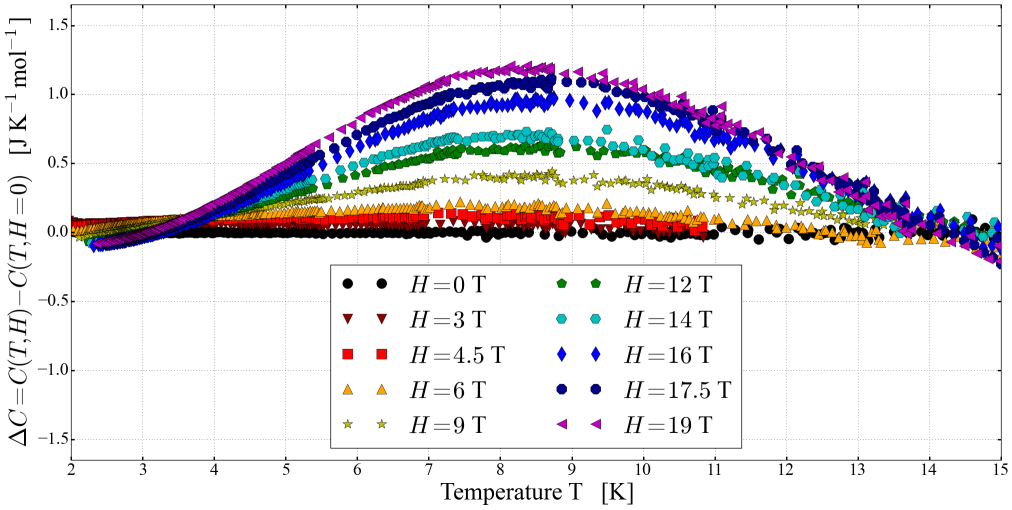

Figure 27: Difference $\Delta C = C(T,H) - C(T,0)$ of $Ba_{0.1}Sr_{2.9}Cr_2O_8$ as a function of the temperature T for different magnetic fields H.

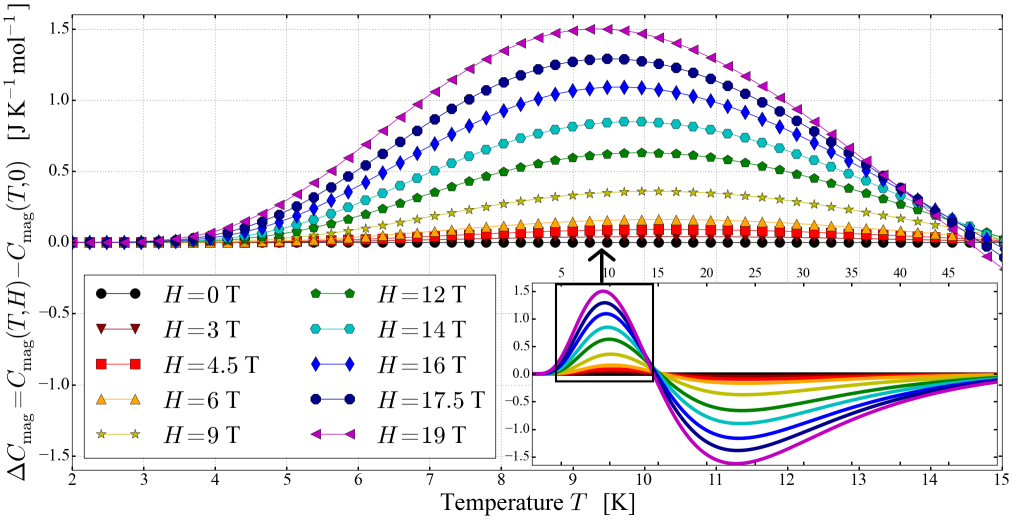

Figure 28: Theoretical difference $\Delta C_{\mathrm{mag}} = C_{\mathrm{mag}}(T,H) - C_{\mathrm{mag}}(T,0)$ as a function of the temperature T for different magnetic fields H. In the inset, ΔC_{mag} is shown in a bigger range of temperatures. The curves were obtained with the energy gap $\Delta = 5.2\,\mathrm{meV}$ and g-factor $g = 1.94$.

additional terms due to impurities (Figure 29). The effective gap is $\Delta_{\text{eff}} = (5.34 \pm 0.01)\,\text{meV}$ and the fraction of dimers is $n_d = 1.00 \pm 0.01$. The fit shows that the impurities contribute to the heat capacity even for temperatures higher than 20 K. Comparing the theoretical curves with the experimental data for $H > 0$ (Figures 46, 47, 48, 49, in Appendix), we noted that the additional contributions (C_{imp}) are magnetic field dependent as well. This explains the negative values of ΔC at low temperatures and the discrepancy between ΔC_{mag} and ΔC. Therefore, the effective gap can be estimated if the impurity are known, or by measuring the heat capacity in a larger temperature range ($2 - 50\,\text{K}$). Indeed, at higher temperatures ($T > 20\,\text{K}$), the additional contributions C_{imp} should vanish.

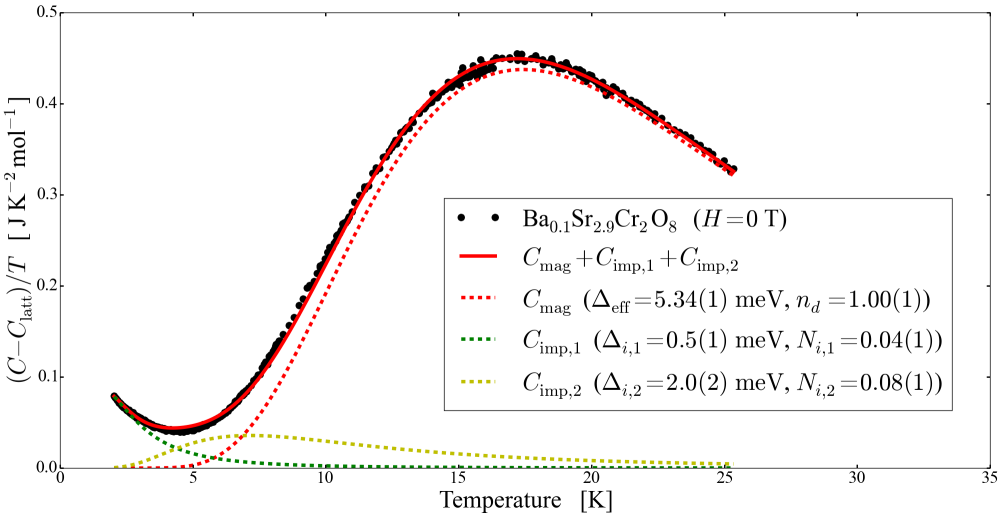

Figure 29: Residual heat capacity $(C - C_{\text{latt}})/T$ of $Ba_{0.1}Sr_{2.9}Cr_2O_8$ as a function of the temperature T ($H = 0$). The fit (red solid line) is given by the sum of three contributions: one magnetic and two impurities terms. The dashed lines represent the single terms.

5 Conclusion

To investigate the adequacy of the heat capacity measurements as a method to estimate the spin gap, we prepared polycrystalline samples of $Ba_{3-x}Sr_xCr_2O_8$ ($0 \leq x \leq 3$). We measured the heat capacity with a PPMS (relaxation calorimetry) and fitted the data with the theoretical model

$$C = C_{\text{latt}} + C_{\text{oo}} + C_{\text{mag}}. \tag{40}$$

After subtraction of the lattice and orbital contributions, we noted that the data were not well described by the Schottky anomaly (isolated spin dimer approximation). The data show a tail amenable to another Schottky anomaly, so we added an additional term (C_{imp}) to the model. This term consist of a Schottky anomaly for a two-level system with energy gap Δ_i. In some cases, a single term was not enough to fit the data well, so we added two contributions. For $Sr_3Cr_2O_8$, we estimate the effective gap $\Delta_{\text{eff}}^{\text{G}}(x=3) = (5.42 \pm 0.05)\,\text{meV}$ for the sample (G), and $\Delta_{\text{eff}}^{\text{M}}(x=3) = (5.50 \pm 0.08)\,\text{meV}$ for the sample (M). This result agrees with a previous publication, which reported a quasi non-dispersive magnetic excitation at 5.4 meV [13] (estimated by INS). However, a magnetic scattering experiment determined the spin gap $\Delta = 40\,\text{K}$ (3.45 meV), a value significantly lower than our result [33]. Analogously, Quintero-Castro *et al.* reported a magnetic excitation centered at 5.5 meV with the energy gap $\Delta = 3.5\,\text{meV}$ [3] (determined by INS). [2] From these results, we confirm that the gap Δ_{eff}, which we assessed by the heat capacity measurement, is not the spin gap Δ. Instead, it corresponds to an energy in the center of the band. The measurement of Δ_{eff} for $Ba_3Cr_2O_8$ supports this hypothesis. For this compound, we measured the values $\Delta_{\text{eff}}^{\text{G}}(x=0) = (2.38 \pm 0.05)\,\text{meV}$ and $\Delta_{\text{eff}}^{\text{M}}(x=0) = (2.42 \pm 0.05)\,\text{meV}$. These values are in agreement with the result of Kofu *et al.* [5]. They performed another INS experiment, observing a prominent excitation at 2.2 meV. Moreover, Nakajima *et al.* [4] performed high-field magnetisation measurements and estimated the energy gap $\Delta = 16.1$ K (1.4 meV) from the critical magnetic field ($\Delta = g\mu_{\text{B}}H_{\text{c}}$, $g = 2$). Once again, the effective gap is larger than the spin gap, while it is comparable to the center of the magnetic excitation. Interestingly, the effective gaps have magnitude similar to the interaction constants, rather than to the spin gap. In fact, the interaction constants of these compounds are $J_0(x=3) = 5.55\,\text{meV}$ [3] and $J_0(x=0) = 2.38\,\text{meV}$ [6].

This result shows that the heat capacity is only slightly affected by the inter-dimer interactions, since the values obtained almost reflect the isolated dimer approximation, *i. e.* $\Delta_{\text{eff}} \approx J_0$. It is probable that when considering the excitation of the spin dimers like a statistical process, the value of Δ_{eff} corresponds to a weighted mean value of the energies required for the excitations. For the intermediate Sr contents x ($0 < x < 3$), we did not find any references about the energy gap, so we compared our values of the effective gap with the magnitude of the exchange constants measured by a magnetisation measurement [7]. We measured $\Delta_{\text{eff}}(x=2.7) = (4.91 \pm 0.06)\,\text{meV}$ and $\Delta_{\text{eff}}(x=1.5) = (4.1 \pm 0.1)\,\text{meV}$, while $J_0(x=2.7) \approx 4.1$ meV and $J_0(x=1.5) \approx 1.6\,\text{meV}$. Surprisingly, for both compounds, the exchange constants is smaller than the values of Δ_{eff}. This result is in contrast with our expectation ($\Delta_{\text{eff}} \leq J_0$) and cannot be interpreted without further measurements. Furthermore, the magnetic contribution of $Ba_{1.5}Sr_{1.5}Cr_2O_8$ is about 60 % smaller than in the other compounds, indicating the presence of non-dimerized Cr^{5+} ions. To sum up these results, we report the energy gaps and the exchange constants as a function of the Sr content x (Figure 30). The increase of Δ_{eff} in the region $2.7 < x < 3$ is similar to the increase of J_0. In contrast, the effective gap of $x = 1.5$ apparently lies on a hypothetical line that connects the gap values of $x = 0$ and $x = 3$.

Finally, we analysed the heat capacity in different magnetic fields $\Delta C(T,H) = C(T,H) - C(T,0)$ for $x = 2.9$. The data should be fitted by the difference between the magnetic contribution with and without magnetic field, since it is the unique factor in the theoretical model that is field dependent. The theoretical curve ΔC_{mag} is given by Equation (23), using the energies $\varepsilon_{0,1,2,3} = \{0,\ \Delta_{\text{eff}} - g\mu_{\text{B}}H,\ \Delta_{\text{eff}},\ \Delta_{\text{eff}} + g\mu_{\text{B}}H\}$. The Landé-factor ($g = 1.94$) was determined by ESR [30] for both $Sr_3Cr_2O_8$ and $Ba_3Cr_2O_8$, thus the fit was performed with a single free parameter, Δ_{eff}. However, it was not possible to obtain a good fit, because of some additional contributions. We attribute this to the presence of some level-system that are magnetic field dependent too ($C_{\text{imp}}(T,H)$). Therefore, we fitted the data $C(T,0)$ to obtain the magnitude of the gap and to analyse the impurity contributions. The resulting effective gap is $\Delta_{\text{eff}} = (5.34 \pm 0.01)\,\text{meV}$, which is similar to the interaction constant $J_0(x=2.9) \approx 5.327\,\text{meV}$ determined by INS [26]. We estimate that the impurities contribute to the heat capacity even at temperatures higher than 20 K. In addition, the fit of the data with magnetic field ($H > 0$) suggest that the theoretical model of $C(T,0)$ is not exact, because the magnetic dependence of the impurities cannot be described by the function used for C_{imp}. Unfortunately, the restricted range of temperatures does not allow a more precise analysis.

[2] The center of the magnetic excitation was determined by plotting the intensity of the scattered neutron as a function of the wave vector transfer $|Q|$ and energy transfer E.

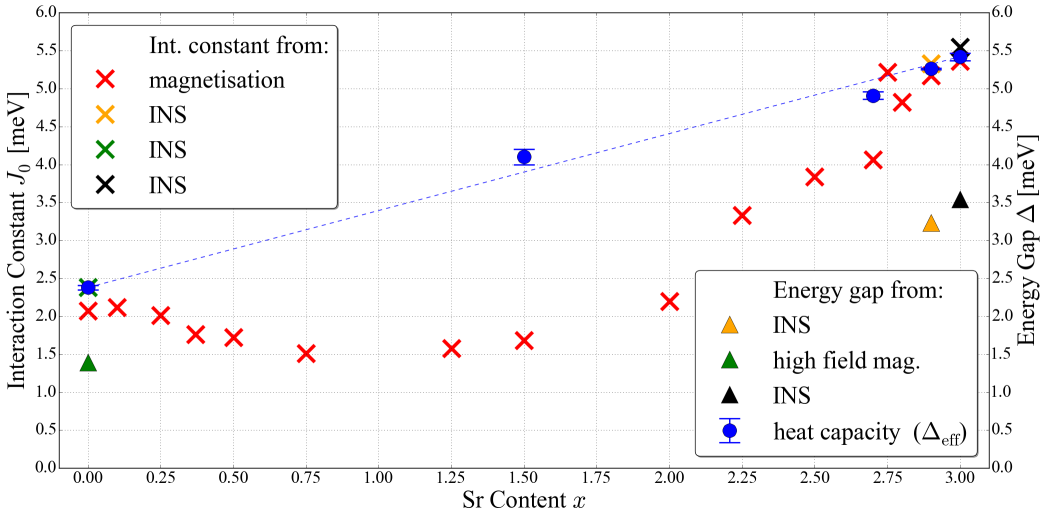

Figure 30: Interaction constant J_0 (plus symbol) [7, 6, 3] and Energy gap Δ (triangle) [3, 4, 26] as a function of the Sr content x. The dashed line is a hypothetical connection between different Δ values.

In conclusion, the heat capacity provides reliable results for the scale magnetic excitation of $x = 0$ and $x = 3$. However, it is not possible to estimate the energy gap with this technique, because the Schottky anomaly is not enough sensitive on the dispersion of the excited state. Since the experimental data are well described by the isolated dimer approximation, the effective gap could be an approximation of the exchange constant J_0. In future, additional experiments are required to determine the behaviour of the effective energy gap for intermediate Sr contents and to verify the discrepancy between heat capacity and magnetisation measurements. In addition to that, we suppose that a systematic measurement of the heat capacity with and without magnetic field would lead to more precise results. Indeed, such method does not require fitting the lattice and the orbital contributions, which are not well defined for the intermediate Sr content. Since there is some unknown contribution in the spin dimer system $Ba_{3-x}Sr_xCr_2O_8$, we suggest to measure a large range of temperatures ($2 - 50\,K$) in order to study the magnetic contribution and the impurities as well. Furthermore, the investigation of a possible relation between the effective gap and the spin gap could be a proposal for a new study.

References

[1] A. A. Aczel, H. A. Dabkowska, P. R. Provencher, and G. M. Luke, *Crystal growth and characterization of the new spin dimer system $Ba_3Cr_2O_8$*, Journal of crystal growth 310, 870-873, 2008.

[2] Y. Singh and D. C. Johnston, *Singlet ground state in the spin-1/2 dimer compound $Sr_3Cr_2O_8$*, arXiv:cond-mat/072309v2, 2007.

[3] D. L. Quintero-Castro, B. Lake, E. M. Wheeler, A. T. M. N. Islam, T. Gaudi, K. C. Rule, Z. Izaola, M. Russina, K. Kiefer and Y. Skourski, *Magnetic excitations of the gapped quantum spin dimer antiferromagnet $Sr_3Cr_2O_8$*, Phys. Rev. B 81, 014415, 2010.

[4] T. Nakajima, H. Mitamura and Y. Ueda, *Singlet Ground State and Magnetic Interactions in New Spin Dimer System $Ba_3Cr_2O_8$*, Journal of Physical Society of Japan, 2006.

[5] M. Kofu, J.-H. Kim, C. Lee, B. Lake, Y. Qiu, H. Ueda, and Y. Ueda, *Magnetic excitations in a quantum spin dimer system $Ba_3Cr_2O_8$*, APS Meeting Abstracts, 2008.

[6] M. Kofu, J.-H. Kim, S. Ji, S.-H. Lee, H. Ueda, Y. Qiu, H.-J. Kang, M. A. Green and Y. Ueda, *Weakly Coupled $s = 1/2$ Quantum Spin Singlets in $Ba_3Cr_2O_8$*, Phys. Rev. Lett. 102, 037206, 2009.

[7] E. Grundmann, *Tuning the Bose-Einstein Condensation in Spin Dimer Quantum Magnets*, Mathematische-naturwissenschaftliche Fakultät der Universität Zürich, 2014.

[8] E. A. Cornell and C. E. Wieman, *Nobel Lecture: Bose-Einstein condensation in a dilute gas, the first 70 years and some recent experiments*, Rev. Mod. Phys. 74, 2002.

[9] T. Nikuni, M. Oshikawa, A. Oosawa, and H. Tanaka, *Bose-Einstein Condensation of Dilute Magnons in $TlCuCl_3$*, Phys. Rev. Lett. 84, Number 25 2000.

[10] T. Dodds, B. J. Yang, and Y. B. Kim, *Theory of magneti-field-induced Bose-Einstein condensation of triplons in $Ba_3Cr_2O_8$*, Phys. Rev. B81, 054412, 2010.

[11] A. A. Aczel, Y. Kohama, M. Jaime, K. Ninios, H. B. Chan, L. Balicas, H. A. Dabkowska, and G. M. Luke, *Bose-Einstein condensation of triplons in $Ba_3Cr_2O_8$* Phys. Rev. B79, 100409(R), 2009.

[12] A. A. Aczel, Y. Kohama, C. Marcenat, F. Weickert, M. Jaime, O. E. Ayala-Valenzuela, R. D. McDonald, S. D. Selesnic, H. A. Dabkowska, and G. M. Luke, *Field induced Bose-Einstein condensation of triplons up to 8 K in $Sr_3Cr_2O_8$* arXiv:0908.3049v3 2009.

[13] L. C. Chapon, C. Stock, P. G. Radaelli and C. Martin, *Orbital ordering promotes weakly-interacting $S = 1/2$ dimers in the triangular lattice compound $Sr_3Cr_2O_8$*, arXiv:0807.0877v2, 2008.

[14] H. Grundmann, A. Schilling, M. Medarde, D. Sheptyakov, *Influence of disorder on the structural phase transition and magnetic interactions in $Ba_{3-x}Sr_xCr_2O_8$*, Phys. Rev. B90, 075101, 2014.

[15] Prof. Dr. T. German, *Theorie der Wärme (Mitschrift)*, Universität Zürich, 2015.

[16] S. L. Chaplot, R. Mittal, and N. Choudhury, *Thermodynamic Properties of Solids*, Wiley-VCH, Weinheim, 2010.

[17] Zhe Wang, M. Schmidt, A. Günther, S. Schaile, N. Pascher, F. Mayr, Y. Gonscharov, D. L. Quintero-Castro, A. T. M. N. Islam, B. Lake, H.-A. Krug von Nidda, A. Loidl and J. Deisenhofer, *Orbital fluctuations and orbital order below the Jahn-Teller transition in $Sr_3Cr_2O_8$*, Phys. Rev B83, 201102(R), 2011.

[18] Zhe Wang, M. Schmidt, A. Günther, F. Mayr, Y. Wan, S.-H. Lee, H. Ueda, Y. Ueda, A. Loidl and J. Deisenhofer, *Infrared phonons and specific heat in the gapped quantum magnet $Ba_3Cr_2O_8$*, Phys. Rev. B85, 224304, 2012.

[19] J. Sólyom, *Fundamental of the physics of solids*, Springer Verlag, Berlin, 2007.

[20] C. Kittel, *Einführung in die Festkörperphysik*, Oldenburg Verlag, München, 2013.

[21] R. Gross, A. Marx, *Festkörperphysik*, Walter de Gruyter, Berlin, 2014.

[22] Prof. Dr. Andreas Schilling, *Private communication*, 2016.

[23] D. L. Quintero-Castro, *Neutron Scattering Investigation on 3d and 4f Frustrated Magnetic Insulators*, Helmholtz Zentrum Berlin, 2011.

[24] J. Jensen, D. L. Quintero-Castro, A. T. M. N. Islam, K. C. Rule, M. Mansson, and B. Lake, *Lineshape of the singlet-triplet excitations in the dimer system $Sr_3Cr_2O_8$ to first order in the high-density $1/z$ expansion*, Phys. Rev. B 89, 134407, 2014.

[25] Z. Wang, *Terahertz and Infrared Spectroscopy on Low-Dimensional Quantum Magnets*, Mathematisch-Naturwissenschaftlich-Technischen Fakultät der Universität Augsburg, 2015.

[26] A. Gazizulina *et al.*, Article in process, physics institute, University of Zurich, 2017.

[27] P. Kretz, *Jahn-Teller Effect in $Ba_{3-x}Sr_xCr_2O_8$*, Bachelorarbeit, Physikinstitut, University of Zurich, 2015.

[28] G. Ventura and M. Perfetti, *Thermal properties of solids at room and cryogenic temperatures*, Sringer edition, 2014.

[29] *Physical Property Measurement System, Heat Capacity Option User's Manual*, Quantum Design, San Diego 2004.

[30] Z. Wang, D. Kamenskyji, O. Cépas, M. Schmidt, D. L. Quintero-Castro, A. T. M. N. Islam, B. Lake, A. A. Aczel, H. A. Dabkovska, A. B. Dabkovski, G. M. Luke, Y. Wan, A. Loidl, M. Ozerov, J. Wosnitza, S.A. Zvyagin, and J. Deisenhofer, *High-field electron spin resonance spectroscopy of singlet-triplet transitions in the spin-dimer systems $Sr_3Cr_2O_8$ and $Ba_3Cr_2O_8$*, Phys. Rev. B89, 174406, 2014.

[31] M. Kofu, H. Ueda, H. Nojiri, Y. Oshima, T. Zenmoto, K. C. Rule, S. Gerischer, B. Lake, C. D. Batista, Y. Ueda, and S.-H. Lee, *Magnetic-Field Induced Phase Transition in a Weakly Coupled $s = 1/2$ Quantum Spin Dimer System $Ba_3Cr_2O_8$*, Phys. Rev. Lett. 102, 177204, 2009.

[32] D. Kamenskyi, J. Wosnitza, J. Krzystek, A. A. Aczel. H. A. Dabkovska, A. B. Dabkovska, G. M. Luke, S. A. Zvyagin, *High-field ESR Studies of the Quantum Spin Dimer System $Ba_3Cr_2O_8$*, J Low Temp Phys 170:231-235, 2013.

[33] D. Wulferding, P. Lemmens, K. Y. Choi, V. Gnezdilov, Y. G. Pashkevich, J. Deisenhofer, D. Quintero-Castro, A. T. M. N. Islam, and B. Lake, *Coupled spin-lattice fluctuations in a compound with orbital degrees of freedom: The Cr-based dimer system $Sr_3Cr_2O_8$*, Phys. Rev. B84, 064419, 2011.

A Appendix

Interpolation method

$Ba_3Cr_2O_8$ and $Sr_3Cr_2O_8$ are two compounds with the same crystal structure and in principle the same bond. The difference between them is essentially the mass and the volume of the unit cell. They can be converted into each other, through the solid solution $Ba_{3-x}Sr_xCr_2O_8$ by chemical substitution of Sr respectively Ba atoms.

According to the simple spring model of solids, the atoms are bound by a force, which obey the Hook's law $F = -fr$, where f is the spring constant and r is the distance between the atoms. The mean frequency of the ion's vibrations is given by $\omega = \sqrt{f/m}$. The Debye temperature is proportional to the Debye frequency

$$\Theta_\mathrm{D} = \frac{\hbar\omega_\mathrm{D}}{k_\mathrm{B}} \propto \sqrt{\frac{f}{m}}. \tag{41}$$

We can estimate the spring constant f using the definition $F = -\frac{dU(r)}{dr}$ for a spherical symmetric potential U. A good approximation of the ionic potential is given by the *Mie-ansatz*

$$U(r) = -\frac{a}{r} + \frac{b}{r^n}, \tag{42}$$

where the first term indicates the Coulomb term and the second represents the repulsion term, a and b are constants. Since r_0 is the equilibrium point, the necessary condition of a minimum $\frac{dU}{dr}\big|_{r=r_0} = 0$ must be fulfilled. This condition leads to a first equation

$$\frac{a}{r_0^2} - \frac{nb}{r_0^{n+1}} = 0. \tag{43}$$

According to the Hook's law, the second derivative of the potential at the equilibrium point is equal to the spring constant, thus

$$f = \left.\frac{d^2U}{dr^2}\right|_{r=r_0} = -\frac{2a}{r_0^3} + \frac{n(n+1)b}{r_0^{n+2}}. \tag{44}$$

The equation (43) in (44) gives

$$f = \frac{(n-1)a}{r_0^3}. \tag{45}$$

The spring constant depend on r_0^{-3}, consequently it is proportional to the inverse of the unit cell volume V_E of the crystal and the Debye temperature scales with

$$\Theta_\mathrm{D} \propto \frac{1}{\sqrt{m \cdot V_\mathrm{E}}}, \tag{46}$$

where for m one can also use the molar mass.

If we plot the heat capacity vs. T/Θ, the single terms of the lattice contribution of $Ba_{3-x}Sr_xCr_2O_8$ should have the same shape for all x ($0 < x < 3$). If we plot the heat capacity vs. T/Θ the curve is the same for all x (Sr content). This means, that the compound A ($Sr_3Cr_2O_8$) and B ($Ba_3Cr_2O_8$) have the same value of the molar heat capacity at two different temperatures T_A and T_B. Because of the relation (46), the temperatures are correlated via

$$T_B = T_A\sqrt{\frac{M_A V_A}{M_B V_B}}, \tag{47}$$

where $M_{A,B}$ are the molar masses and $V_{A,B}$ are the unit cell volumes of the compounds A and B.

For two compounds with similar physical and chemical properties the ratio $\Delta C_{AB}/C_B \approx \Delta C_{AB}/C_A$ is very small, where $\Delta C_{AB} = C_B - C_A$. For this reason the difference between the temperatures T_A and T_B is small and the curve of the heat capacity can be linearised in this interval of temperatures (Figure 31).

From the known heat capacity $C_{A,B}$ one can derive the heat capacity for the intermediate Sr content ($0 < x < 3$) via

$$C(T) = C_B - \varepsilon\Delta C_{AB} = \varepsilon C_A(T) + (1-\varepsilon)C_B(T). \tag{48}$$

The geometrical relation between the catheti of similar triangle (Figure 31, inset) leads to

$$\varepsilon = \frac{T - T_A}{T_B - T_A} = \frac{(M_x V_x)^{-1/2} - (M_A V_A)^{-1/2}}{(M_B V_B)^{-1/2} - (M_A V_A)^{-1/2}}, \tag{49}$$

where in the last step we used the equation (47). Here M_x and V_x are the molar mass and unit cell volume of $Ba_{3-x}Sr_xCr_2O_8$. The volume of the unit cell can be determined by X-ray diffraction analysis, or can be approximated applying the Vegard's law, i.e. by linear interpolation of the lattice parameters as a function of x.

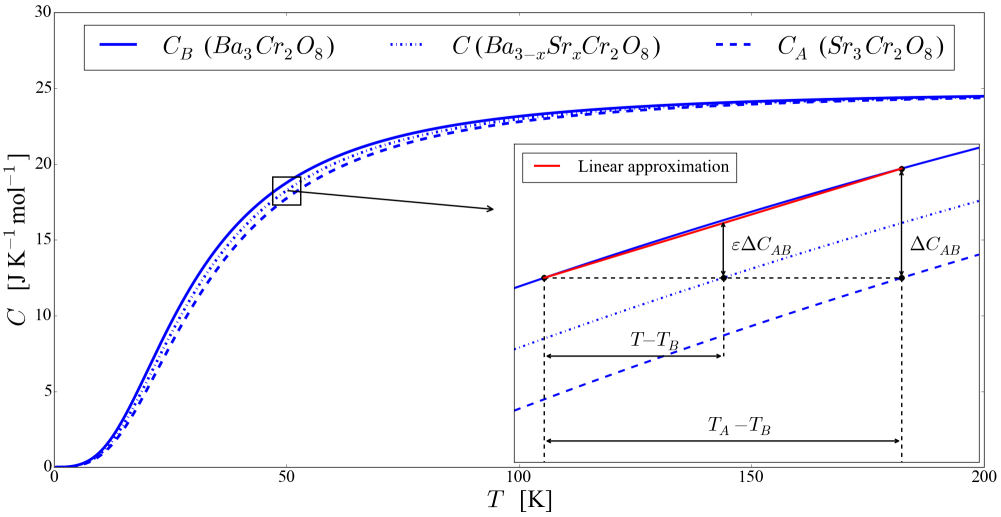

Figure 31: The heat capacity as a function of the temperature described by the Debye model. The inset shows the linear approximation of the heat capacity in a small interval of temperatures.

$Sr_3Cr_2O_8$

X-Ray Diffraction Experiments

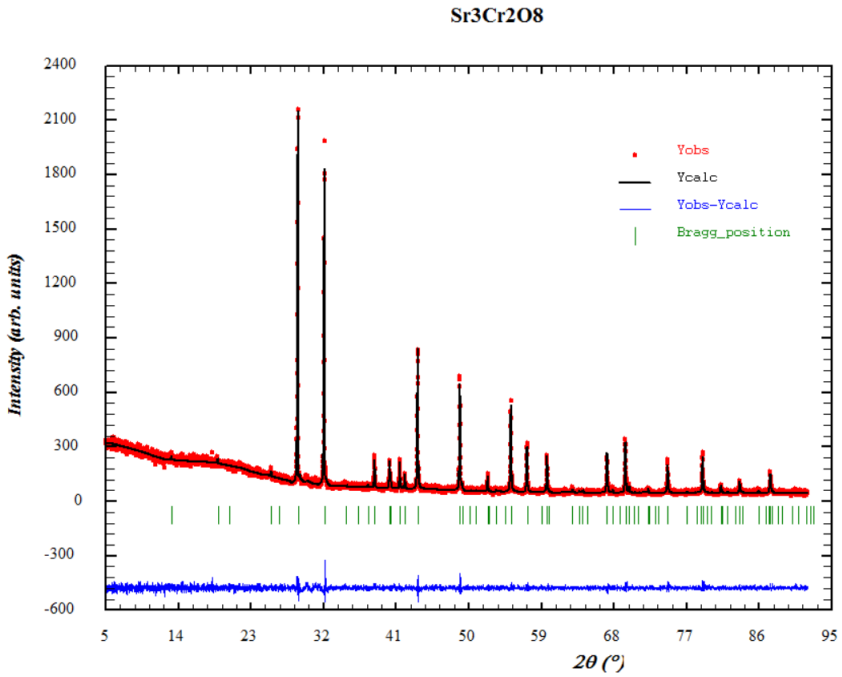

Figure 32: XRD intensity pattern of $Sr_3Cr_2O_8$. The red points are the experimental data. The black solid lines is the theoretical curve for the hexagonal space group $R\bar{3}m$. The blue line is difference between the data and the fit.

Lattice parameters of $Sr_3Cr_2O_8$

a=b (Å)	c (Å)	Measurement method
5.5719(1)	20.1700(4)	X-ray diffraction
5.57071(6)	20.1654(3)	Neutron diffraction [7]

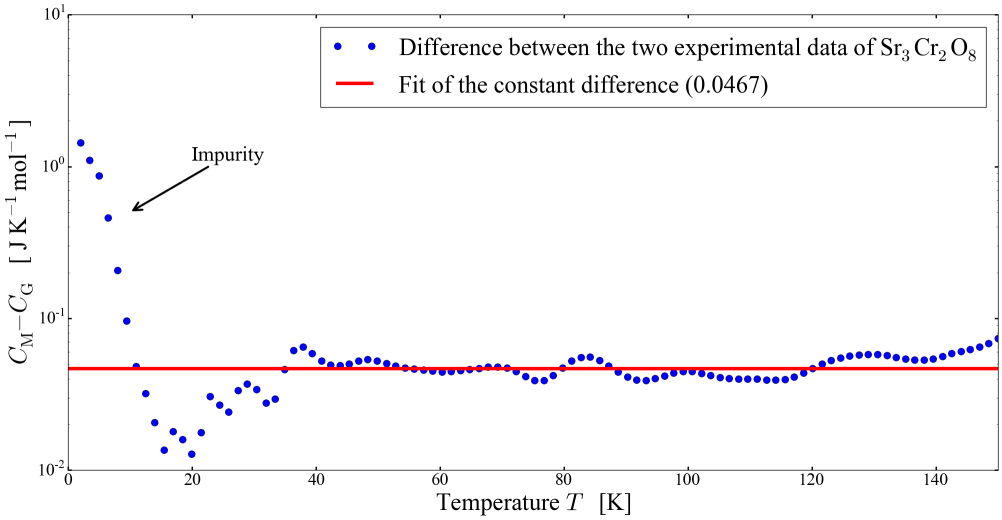

Figure 33: Difference between the molar heat capacity of the samples $Sr_3Cr_2O_8$ (M) and (G) on a semi logarithmic scale. In the range of temperatures $40 - 150$ K, the difference is constant, which means that the experimental data differ from a constant factor: $C_M = (\text{factor}) * C_G$.

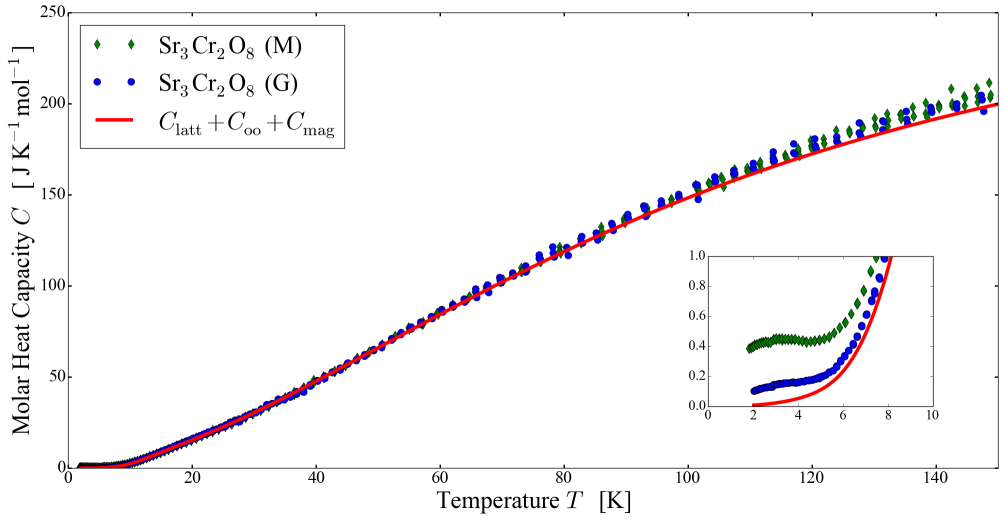

Figure 34: Molar heat capacity C of $Sr_3Cr_2O_8$ as a function of the temperature T. The experimental data were measured for two different samples as reported in Chapter 3. The experimental data of the sample (M) was multiplied by a factor 1.0478. The red line represents the model proposed by Wang et *al* [17]. The model takes into account the lattice, orbital ($\Delta_{\text{oo}} = 33.4$ meV) and magnetic ($\Delta_{\text{eff}} = 5.55$ meV) contributions. The inset show a zoom in the temperature range $0 - 10$ K.

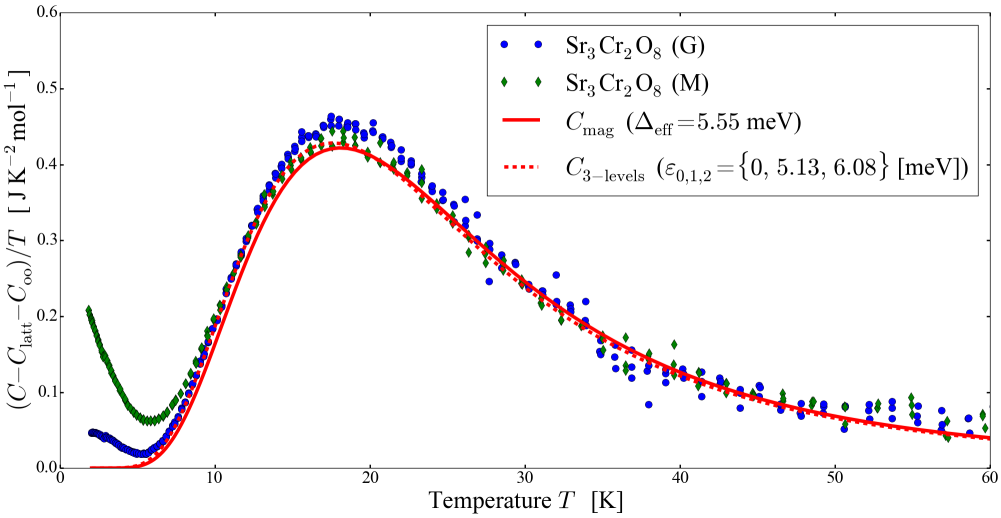

Figure 35: Residual heat capacity $(C - C_{\text{latt}} - C_{\text{oo}})/T$ of $Sr_3Cr_2O_8$ as a function of the temperatures T. The red solid line was obtained with the energy gap $\Delta = 5.55\,\text{meV}$, while the red dashed line represent the theoretical curve for a three-level system(energies reported in the legend).

$Ba_{0.3}Sr_{2.7}Cr_2O_8$

X-Ray Diffraction Experiments

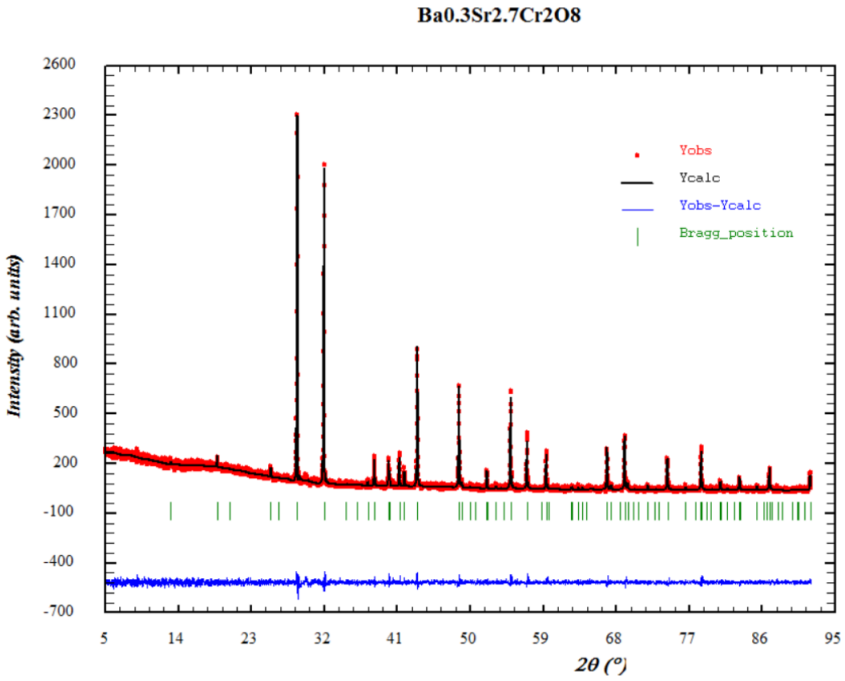

Figure 36: XRD intensity pattern of $Ba_{0.3}Sr_{2.7}Cr_2O_8$. The red points are the experimental data. The black solid lines is the theoretical curve for the hexagonal space group $R\bar{3}m$. The blue line is difference between the data and the fit.

Lattice parameters of $Ba_{0.3}Sr_{2.7}Cr_2O_8$		
a=b (Å)	c (Å)	Measurement method
5.5919(1)	20.2887(4)	X-ray diffraction

Molar Heat Capacity

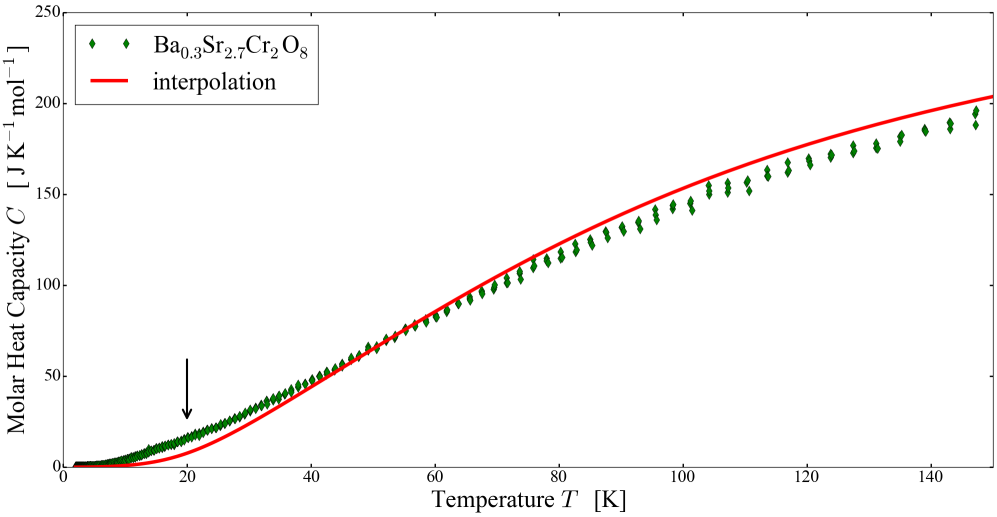

Figure 37: Molar heat capacity C of $Ba_{0.3}Sr_{2.7}Cr_2O_8$ as a function of the temperature T. The red line represents the theoretical model ($C_{\mathrm{latt}} + C_{\mathrm{oo}}$). The lattice contribution was obtained by the interpolation between the heat capacity of $Sr_3Cr_2O_8$ and $Ba_3Cr_2O_8$. The orbital contribution was obtained by using the energy gap $\Delta_{\mathrm{oo}} = 28.1\,\mathrm{meV}$. The magnetic contribution is marked with an arrow.

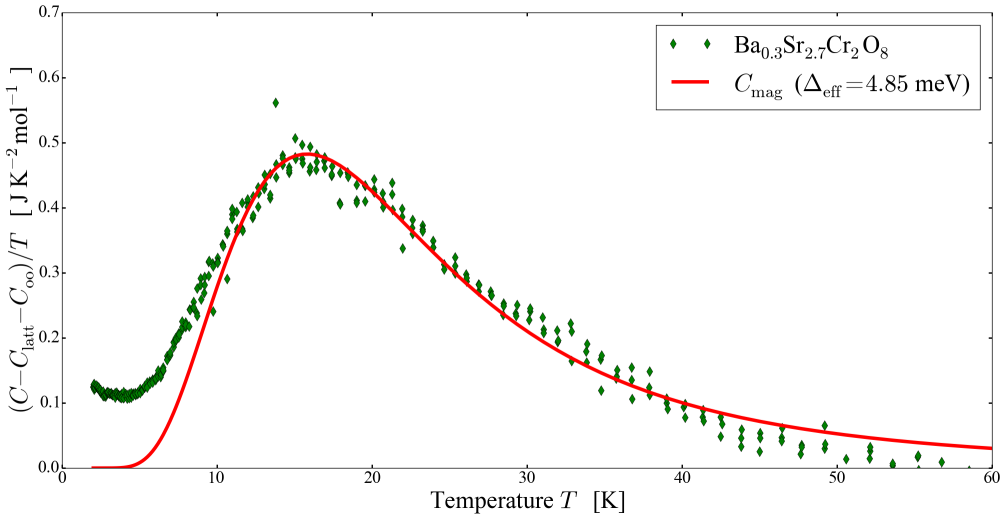

Figure 38: Residual heat capacity $(C - C_{\mathrm{latt}})/T$ of $Ba_{0.3}Sr_{2.7}Cr_2O_8$ as a function of the temperatures T. The theoretical curve (red solid line) represents the magnetic contribution.

$Ba_{1.5}Sr_{1.5}Cr_2O_8$

X-Ray Diffraction Experiments

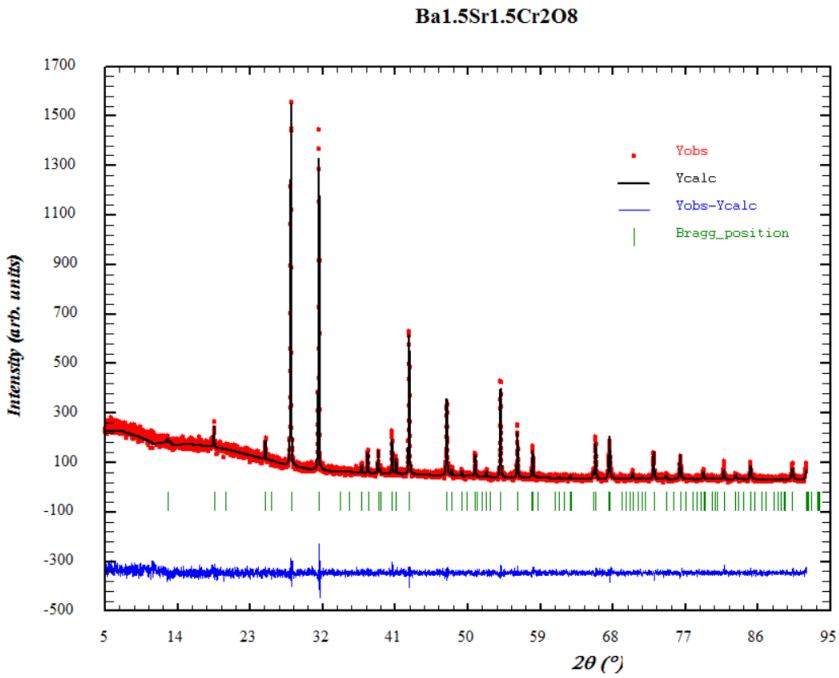

Figure 39: XRD intensity pattern of $Ba_{1.5}Sr_{1.5}Cr_2O_8$. The red points are the experimental data. The black solid lines is the theoretical curve for the hexagonal space group $R\bar{3}m$. The blue line is difference between the data and the fit.

Lattice parameters of $Ba_{1.5}Sr_{1.5}Cr_2O_8$		
a=b (Å)	c (Å)	Measurement method
5.6671(1)	20.8091(6)	X-ray diffraction

Molar Heat Capacity

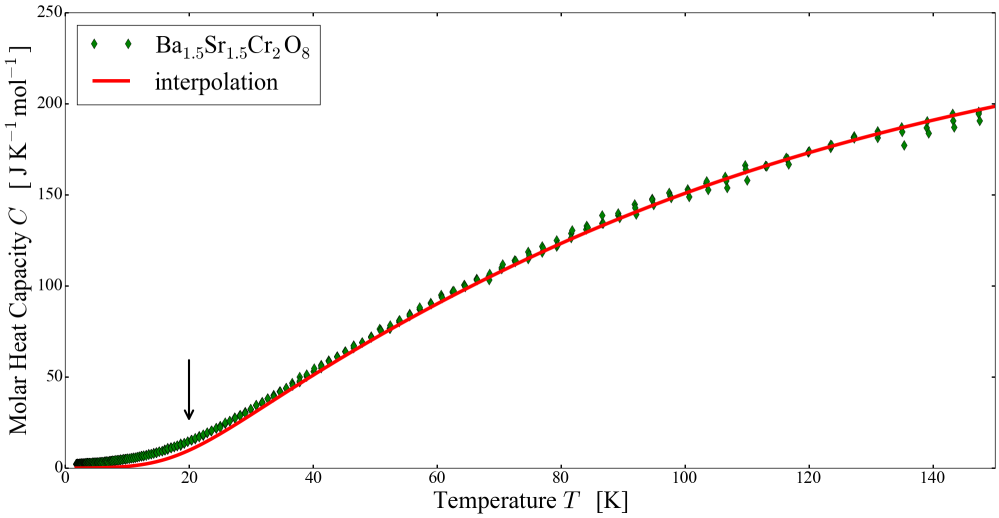

Figure 40: Molar heat capacity C of $Ba_{1.5}Sr_{1.5}Cr_2O_8$ as a function of the temperature T. The theoretical curve (red solid line) is given by the sum of the lattice and orbital contributions. The lattice term was obtained with an interpolation method starting from the heat capacity of the parent compounds $x = 0$ and $x = 3$. The energy gap of the orbital contribution was estimated to be $\Delta_{oo} = 9.3\,\text{meV}$. The magnetic contribution is marked with an arrow.

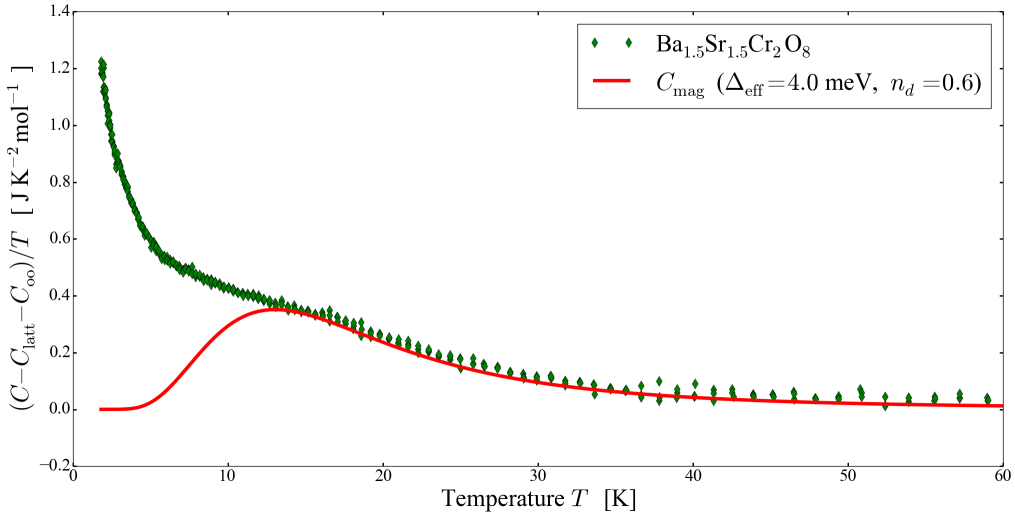

Figure 41: Residual heat capacity $(C - C_{\text{latt}} - C_{\text{oo}})/T$ of $Ba_{1.5}Sr_{1.5}Cr_2O_8$ as a function of the temperatures T. The theoretical curve takes into account only the magnetic contribution, while the data show a prominent tail, indicating the presence of impurities.

$Ba_3Cr_2O_8$

X-Ray Diffraction Experiments

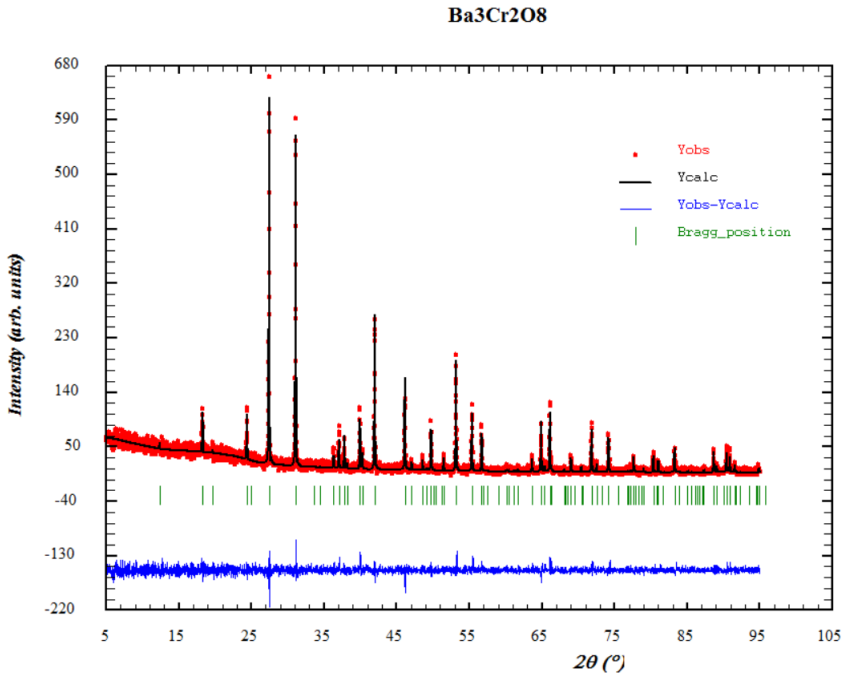

Figure 42: XRD intensity pattern of $Ba_3Cr_2O_8$. The red points are the experimental data. The black solid lines is the theoretical curve for the hexagonal space group $R\bar{3}m$. The blue line is difference between the data and the fit.

Lattice parameters of $Ba_3Cr_2O_8$

a=b (Å)	c (Å)	Measurement method
5.7415(1)	21.3901(6)	X-ray diffraction
5.74038	21.38354	Neutron diffraction [7]

Molar Heat Capacity

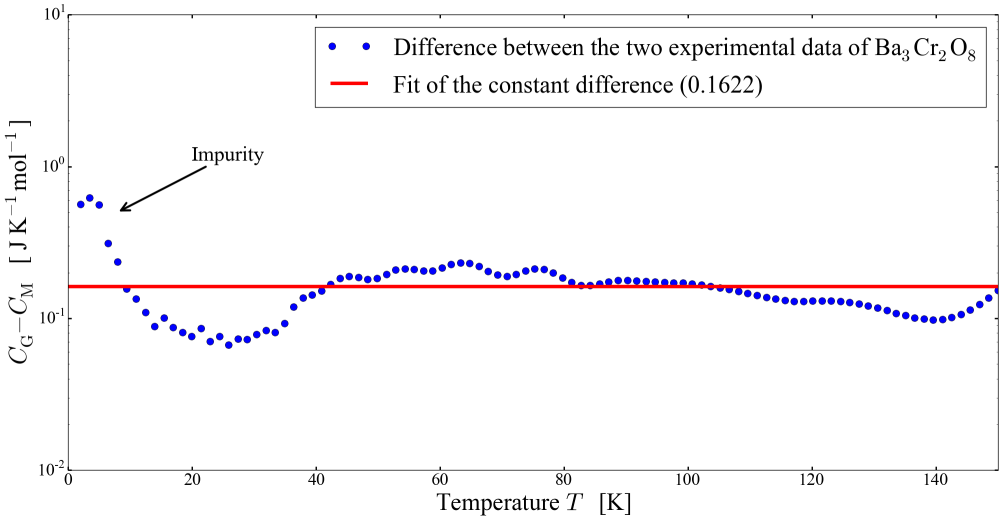

Figure 43: Difference between the molar heat capacity of the samples $Ba_3Cr_2O_8$ (M) and (G) in a semi logarithmic scale.

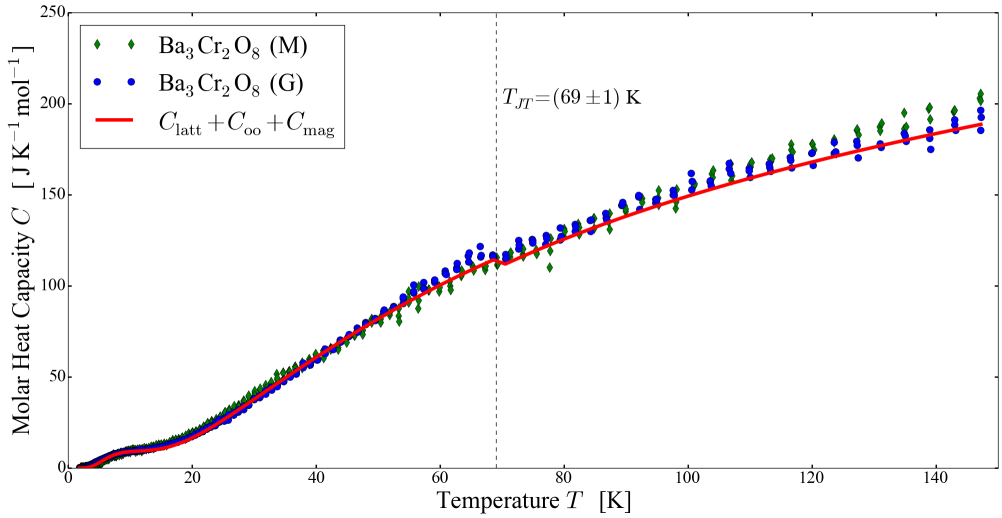

Figure 44: Molar heat capacity C of $Ba_3Cr_2O_8$ as a function of the temperature T (blue dots). At the temperature of 69 K the heat capacity reveals the Jahn-Teller transition. The theoretical curve (red line) represents the model proposed by Wang *et al.* [18]. The model takes into account the lattice, orbital ($\Delta_{oo} = 8.5\,\text{meV}$), and the magnetic contribution ($\Delta_{eff} = 2.38\,\text{meV}$).

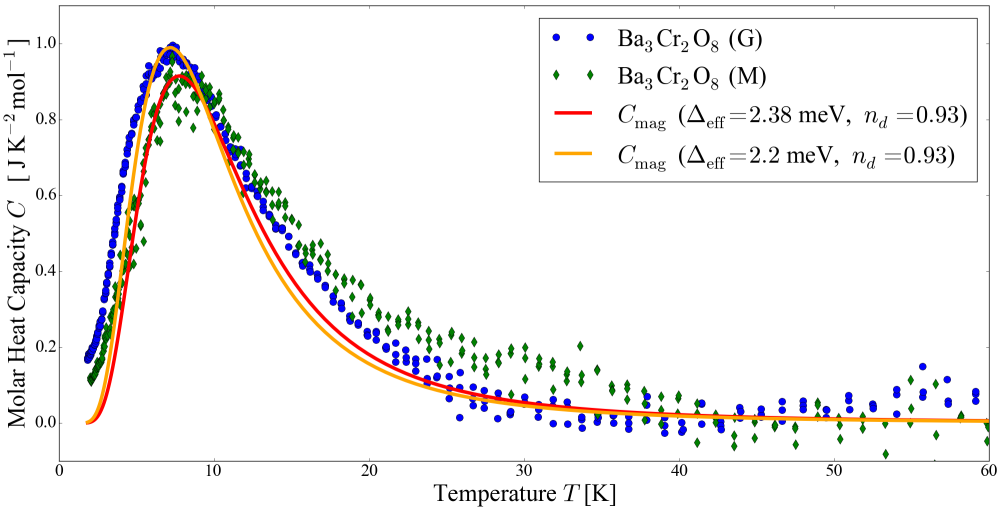

Figure 45: Residual heat capacity $(C - C_{\text{latt}} - C_{\text{oo}})/T$ of $Ba_{0.3}Sr_{2.7}Cr_2O_8$ as a function of the temperature T. The theoretical curves (red and orange solid line) represent the magnetic contribution.

$Ba_{0.1}Sr_{2.9}Cr_2O_8$

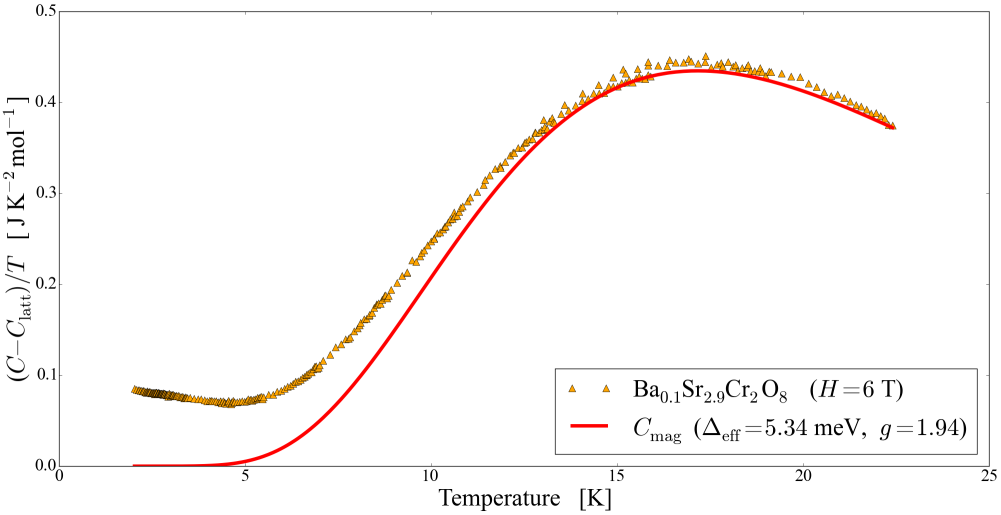

Figure 46: Residual heat capacity $(C - C_{\text{latt}})/T$ of $Ba_{0.1}Sr_{2.9}Cr_2O_8$ as a function of the temperature T for the magnetic field $H = 6\,\text{T}$. The theoretical curve (red solid line) was obtained with the energy gap $\Delta = 5.26\,\text{meV}$ and g-factor $g = 1.94$.

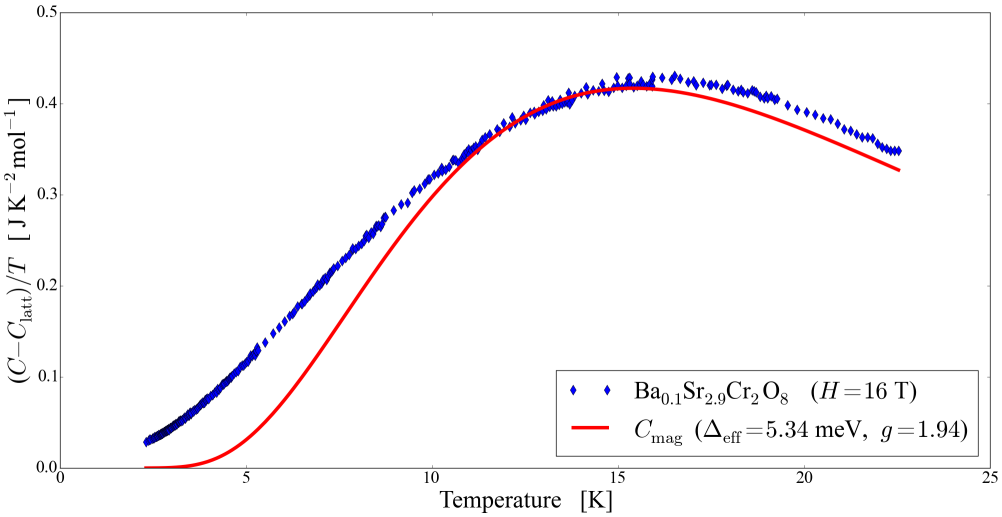

Figure 47: Residual heat capacity $(C - C_{\mathrm{latt}})/T$ of $Ba_{0.1}Sr_{2.9}Cr_2O_8$ as a function of the temperature T for the magnetic field $H = 16\,\mathrm{T}$. The theoretical curve (red solid line) was obtained with the energy gap $\Delta = 5.26\,\mathrm{meV}$ and g-factor $g = 1.94$.

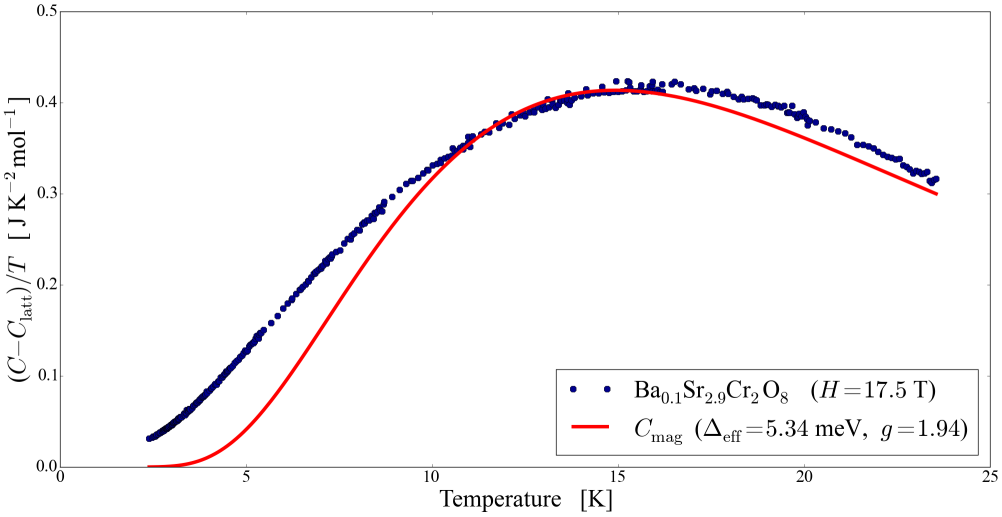

Figure 48: Residual heat capacity $(C - C_{\mathrm{latt}})/T$ of $Ba_{0.1}Sr_{2.9}Cr_2O_8$ as a function of the temperature T for the magnetic field $H = 17.5\,\mathrm{T}$. The theoretical curve (red solid line) was obtained with the energy gap $\Delta = 5.26\,\mathrm{meV}$ and g-factor $g = 1.94$.

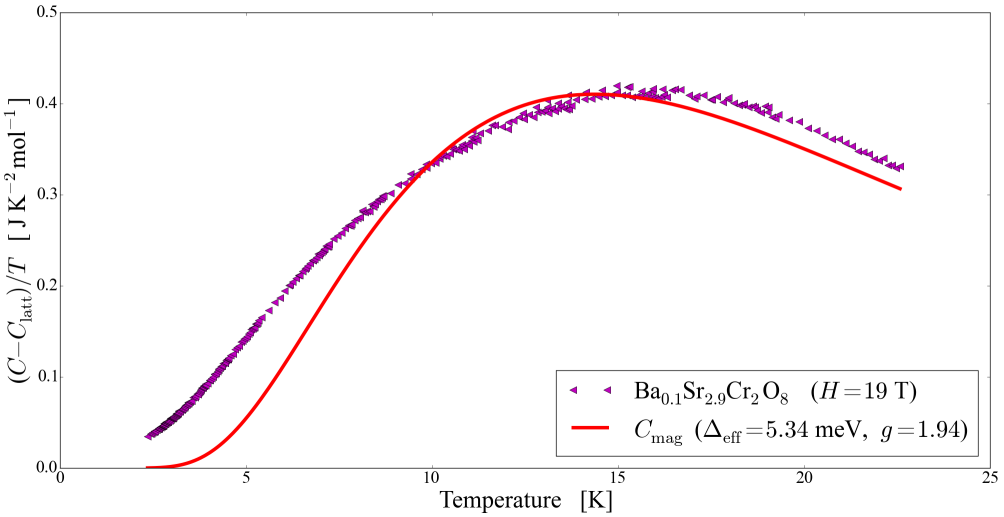

Figure 49: Residual heat capacity $(C - C_{\mathrm{latt}})/T$ of $Ba_{0.1}Sr_{2.9}Cr_2O_8$ as a function of the temperature T for the magnetic field $H = 19\,\mathrm{T}$. The theoretical curve (red solid line) was obtained with the energy gap $\Delta = 5.26\,\mathrm{meV}$ and g-factor $g = 1.94$.